

## Modeling Polarity-Driven Laminar Patterns in Bilayer Tissues with Mixed Signaling Mechanisms\*

Joshua W. Moore<sup>†‡</sup>, Trevor C. Dale<sup>§</sup>, and Thomas E. Woolley<sup>‡</sup>

**Abstract.** Recent advances in high-resolution experimental methods have highlighted the significance of cell signal pathway crosstalk and localized signaling activity in the development and disease of numerous biological systems. The investigation of multiple signal pathways often introduces different methods of cell-cell communication, i.e., contact-based or diffusive signaling, which generates both a spatial and a temporal dependence on cell behaviors. Motivated by cellular mechanisms that control cell-fate decisions in developing bilayer tissues, we use dynamical systems coupled with multilayer graphs to analyze the role of signaling polarity and pathway crosstalk in fine-grain pattern formation of protein activity. Specifically, we study how multilayer graph edge structures and weights influence the layerwise (laminar) patterning of cells in bilayer structures, which are commonly found in glandular tissues. We present sufficient conditions for the existence, uniqueness, and instability of homogeneous cell states in the large-scale spatially discrete dynamical system. Using methods of pattern templating by graph partitioning to generate quotient systems, in combination with concepts from monotone dynamical systems, we exploit the extensive dimensionality reduction to provide existence conditions for the polarity required to induce fine-grain laminar patterns with multiple spatially dependent intracellular components. We then explore the spectral links between the quotient and large-scale dynamical systems to extend the laminar patterning criteria from existence to convergence for sufficiently large amounts of cellular polarity in the large-scale dynamical system, independent of spatial dimension and number of cells in the tissue.

**Key words.** pattern formation, monotone systems, pathway crosstalk, spectral graph theory, cell polarity, interconnected systems

**MSC codes.** 92C15, 37N25

**DOI.** 10.1137/22M1522565

**1. Introduction.** Cell-fate determination is the process of stem, or progenitor, cell commitment to transition to a differentiated state with adapted cellular functions [63]. This process enables the generation of specialized cell populations during organ development as cells propagate through lineage structures with each cell-fate choice. Cell-fate decisions are typically regulated by tightly orchestrated intracellular protein cascades often termed genetic regulatory networks (GRNs) that describe complex intracellular protein interactions that

\*Received by the editors September 15, 2022; accepted for publication (in revised form) by A. Layton June 2, 2023; published electronically October 16, 2023.

<https://doi.org/10.1137/22M1522565>

**Funding:** This work was partially supported by the Welsh government's European Social Fund (ESF). The work of the first author was supported by Knowledge Economy Skills Scholarships (KES2), a pan-Wales higher-level skills initiative led by Bangor University on behalf of the Higher Education sector in Wales.

<sup>†</sup>Wolfson Centre for Mathematical Biology, Mathematical Institute, University of Oxford, Oxford OX2 6GG, UK ([joshua.moore@maths.ox.ac.uk](mailto:joshua.moore@maths.ox.ac.uk)).

<sup>‡</sup>School of Mathematics, Cardiff University, Cardiff CF10 3AT, UK ([daletc@cardiff.ac.uk](mailto:daletc@cardiff.ac.uk)).

<sup>§</sup>School of Biosciences, Cardiff University, Cardiff CF10 3AT, UK ([WoolleyT1@cardiff.ac.uk](mailto:WoolleyT1@cardiff.ac.uk)).

depend on both the local cellular environment and the intrinsic genetic properties of the cell [53]. Subsequently, the investigation of the autonomous spatial organization of cell-fate biomarkers (active proteins for cell-fate regulation) in developing tissues has been of significant interest as a strategy to elucidate the intracellular mechanisms that govern such cellular behavior bifurcations [9, 43, 51].

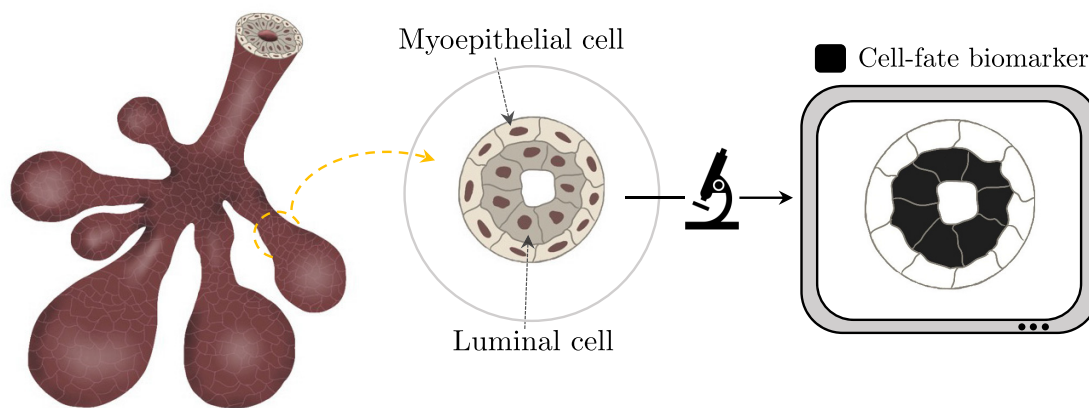
Ductal structures commonly found in glandular tissues possess some of the most simple cell-fate biomarker spatial patterning. Primarily comprised of just two cell types, these tissues produce branching morphologies with a consistent bilayer ring of layerwise contrasting cell types (Figure 1(A)). To form the bilayer rings, undifferentiated cells self-organize to autonomously produce distinct laminar patterns of opposing cell-fate biomarkers to promote the substance transportation functions required of the organ [29]. Common examples of these laminar pattern features can be found in glandular tissues, such as the mammary, salivary, and sweat glands, where the emergence of bilayer cell-type expression initiates the formation of ductal features [18, 54, 60].

Although the spatial patterning of the cell-fate biomarkers can be simple in bilayer tissues, the cellular regulatory mechanisms that generate these cell states are complex, often involving multiple interlinked GRNs, which is referred to as pathway crosstalk [33]. Consequently, pathway crosstalk may induce multiple modes of independent cell-cell communication channels, such as contact-based (juxtacrine) or short-range diffusive (paracrine) protein interactions between local cells [32, 44]. Thus, cells receive local tissue information from a range of sources to consistently select the appropriate cell type for functional ductal formation.

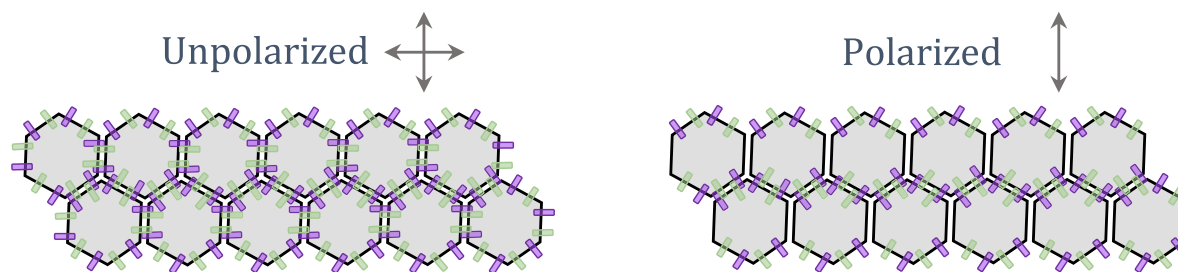
In addition to the rich interactions of intracellular GRNs, a common control mechanism present in developing tissues is cellular polarity. In a broad sense, cell polarity is the asymmetry of the shape or molecular distribution of the cell [13]. In this study, we focus on biochemical asymmetries that are associated with localization of signaling activators and receptors within or on the surface of the cell and refer to this as polarity herein [12]. In general, polarity in cell signaling proteins causes anisotropic communication flow between cells and therefore specifies a niche of adjacent interaction cells, as shown in Figure 1(B) as an example of apical-basal polarity in an epithelial bilayer. The role of polarity is well established in mechanical processes of mammalian development, such as division and adhesion, to ensure consistent morphological features of the tissue during growth [62].

There is growing evidence in a variety of biological systems in which polarity also acts as a spatial coordinator of cell-fate specification and promotes mechanical feedback loops to preserve local cell types for healthy tissue function [47]. However, the precise role polarity has in influencing intracellular kinetics that govern cell-fate choices is widely unknown since cell-cell interactions compound with complex pathway crosstalk [62]. Therefore, in this study, we explore the interplay of polarity and multiple cell-cell signaling mechanisms associated with pathway crosstalk in generating laminar patterns of biomarkers, conforming with the process of cell-fate determination of developing bilayer tissues.

Following Turing's seminal paper in 1952 [61], the majority of theoretical results of pattern formation in developmental biology focus on diffusion-driven instabilities of reaction-diffusion (RD) systems [39, 67]. RD systems rely on the assumption that cells communicate using short-range and/or long-range paracrine signaling mechanisms, namely, the local diffusion of proteins coupled with intracellular kinetics. However, there exists many patternforming



(a) Bilayer structures in glandular tissues.



(b) Cell signaling polarity.

**Figure 1.** Schematic representation of the bilayer cellular architecture of ductal tissues and cellular polarity. (A) Branching tissue structures produce bilayer ducts of layerwise contrasting epithelial cells with the outer and inner layers of myoepithelial and luminal cells, respectively, to facilitate the production and secretion for the transportation of substances such as sweat, saliva, and breast milk [18, 54, 60]. Imaging the ducts for key cell-fate biomarkers highlights the presence of laminar patterns’ intracellular protein expression. Some well-established cell-fate biomarkers are p63 and Notch for myoepithelial and luminal cells in mammary and sweat glands [41, 44]. (B) An example of a contact-dependent signaling mechanism with activators and receptors is represented using purple and green rectangles depicting the effect of layerwise polarity in a bilayer of cells.

biological systems that rely on nondiffusive, juxtacrine communication, such as lateral-inhibition mechanisms, where adjacent cells inhibit each other from converging to the same state, facilitating fine-grain pattern formation [19, 58].

The fundamental differences in paracrine and juxtacrine signaling motivate contrasting modeling approaches. The diffusion process in paracrine signaling extends to a spatial continuum limit, generating small systems of PDEs allowing protein patterns to form over multiple cell lengths to represent phenomena such as morphogen gradients over the tissue [67]. In contrast, the discrete nature of juxtacrine signaling induced by membrane contact necessitates the use of spatially discrete systems of ODEs [64]. Subsequently, these contrasting modeling paradigms restrict the specific continuum and discrete approaches to pattern analysis in systems where both diffusive and nondiffusive mechanisms are present.

Graphs representing spatially discrete analogues of diffusive mechanisms have previously been employed to homogenize the analytical approaches to pattern formation and, further, investigate cell structure on pattern emergence [30]. That is, graph vertices depicting cells and edges are drawn between cells if they are communicating via diffusive proteins. Critically, this approach preserves the concept of cell identity within diffusive models and transforms the systems of PDEs into much larger systems of ODEs, consistent with the juxtacrine model formulation. However, the central theme of pattern analysis is understanding the conditions that yield the degradation of stable homogeneity of the system and is typically conducted via linear stability analysis with coupled spatiotemporal components [16, 49, 65]. Consequently, the high dimension of these ODE descriptions and required nonlinear kinetics of multicellular domains render analytical approaches intractable, which lead to many studies focusing on spatially reduced systems accompanied by numerical simulations for the larger cellular domains [16, 64, 65]. Critically, the analysis conducted on such spatially reduced models has been shown to be insufficient for predicting the types of patterning observed numerically [65], with similar results for cell-resolution discretized diffusive systems [46].

Adopting concepts from systems engineering, the application of interconnected dynamical systems theory was employed in [7] to derive analytic pattern formation conditions for juxtacrine models, independent of the number of cells and therefore the size of the ODE system. Namely, cells were treated as input-output (IO) components within a circuit; i.e., cells receive signals and then produce response signals to other connected cells. This approach recasts the large-scale ODE system in a macroscopic perspective to analyze the behavior of only the directly spatially dependent intracellular proteins using signal transfer functions. Furthermore, extending the low-dimensional quotient representations of graph-coupled dynamical systems as formalized by Golubitsky, Stewart, and coauthors [22, 23, 59] to IO systems, edge symmetries of the cell-cell connectivity graphs were exploited in [52] to develop methods of graph partitioning to form quotient graphs that represent a pattern template. Embedding the intracellular ODE systems defined by the GRNs within these quotient graphs produces a quotient-interconnected dynamical system which is significantly smaller in dimension, specifically when analyzing synchronized intercellular dynamics. Namely, these quotient systems were then used to provide pattern existence conditions for prescribed cellular patterns for interconnected juxtacrine models. These methods of pattern predictions were later extended in [25] and [26] to simultaneously couple diffusive and nondiffusive signaling mechanisms within the interconnected dynamical systems framework using directed multilayer graphs, namely, graphs with unidirectional edges connected to cells with multiple-input and multiple-output signals. However, the influence of edge weights on pattern existence and convergence in these multichannel interconnected systems is yet to be investigated.

The spatial scalability of the interconnected methods of pattern analysis follows from the theory of monotone dynamical systems [6]. Provided the intracellular proteins regulated by the prescribed GRN react monotonically to intercellular stimuli, global dynamics become predictable in a closed-loop system of cells and facilitate the introduction of control theoretic tools for pattern stability [52]. Although the restriction to bipartite connectivity graphs was imposed in [7] and [26] as a sufficient measure to preserve the monotonic behavior of lateral-inhibition models in the large-scale forms, these restrictions limit the biological applications.

Such conditions can be relaxed when seeking pattern existence in quotient systems as demonstrated in [52], but how such behavior translates to the large-scale counterpart is not fully understood.

We have previously analyzed the role of polarity in laminar pattern formation using interconnected methods for a single juxtacrine signaling mechanism [45]. In this study, we generalize and extend these results to include multiple signaling mechanisms of any type using a multilayer graph approach as defined in [26]. Namely, we explore the interplay of multilayer network topology and edge weights in laminar pattern formation in bilayer tissues using dynamical systems of generic competitive kinetics.

Initially, we present conditions for the existence, uniqueness, and instability of a homogeneous steady state (HSS) for a large-scale multiple-input and multiple-output (MIMO) dynamical system which extends the conditions of [26] to yield analytically applicable statements for low-spatial-order intracellular GRNs. Thereafter, we use methods of multilayer graph partitioning to derive polarity conditions for the existence of laminar patterning in large-scale systems. Critically, we demonstrate that the graph commutativity requirements imposed in [26] for simultaneous diagonalization can be relaxed when seeking patterns of only two states, allowing a broader range of quotient connectivities to be explored.

Next, we investigate the spectral links between quotient and large-scale dynamical systems. We demonstrate that positional changes of the eigenvalues associated with laminar patterns in the multigraphs are dependent on the amount of polarity for nonbipartite graphs. We then discuss the implications of spectral rearrangements with respect to bipartite graphs and laminar patterning. Finally, combining our insights from the spectral rearrangements and quotient system analysis, we explore the convergence of laminar patterns in the associated large-scale dynamic systems.

The structure of the study is as follows. In section 2.1, we define the large-scale interconnected dynamical system analyzed in this study. In section 2.2, we present conditions for the existence, uniqueness, and instability of an HSS for a large-scale MIMO dynamical system. Our main results are presented in section 3, where we introduce the necessary results from monotone dynamical systems in section 3.1 and then present conditions for the existence of laminar patterning in section 3.2. In section 3.3, we demonstrate that positional changes of the eigenvalues associated with laminar patterns in the multigraphs are dependent on the amount of polarity for nonbipartite graphs. Finally, in section 3.4, we present sufficient polarity-dependent conditions for the convergence of laminar patterns in the large-scale systems.

**2. Existence of cellular heterogeneity.** In this section, we are interested in deriving conditions for the existence and instability of an HSS of a large-scale dynamical system that describes intracellular kinetics within a tissue of cells. First, we define the types of interconnected dynamical systems considered in this study, namely, coupling the multiple input and output signal dynamics of individual cells using weighted connectivity graphs associated with each respective signaling mechanism. Thereafter, we exploit the repetitive structure of large-scale interconnected dynamical systems to provide analytically tractable conditions for the existence, uniqueness, and stability of the HSS that is necessary for the investigation of polarity-driven cellular heterogeneity.

**2.1. The signal polarity interconnected system for bilayer geometries with multiple signal mechanisms.** Consider a large-scale interconnected dynamical systems representing  $N$  spatially discrete cells, each containing  $n$  intracellular proteins. Namely, for each cell  $i \in \{1, \dots, N\}$ , let  $\mathbf{x}_i = [x_{i,1}, \dots, x_{i,n}]^T \in X \subset \mathbb{R}_{\geq 0}^n$  be the concentration of the intracellular proteins. The cellular signal inputs and outputs are defined by  $\mathbf{u}_i = [u_{i,1}, \dots, u_{i,r}]^T$ ,  $\mathbf{y}_i = [y_{i,1}, \dots, y_{i,r}]^T \in U, Y \subset \mathbb{R}_{\geq 0}^r$ , respectively, for  $1 \leq r \leq n$ . The interconnected ODE system has the form

$$(2.1) \quad \dot{\mathbf{x}}_i = \mathbf{f}(\mathbf{x}_i, \mathbf{u}_i),$$

$$(2.2) \quad \mathbf{y}_i = \mathbf{h}(\mathbf{x}_i),$$

where  $\dot{\mathbf{x}}_i$  represents the derivative with respect to time. The function  $\mathbf{f}: X \times U \rightarrow X$  defines the intracellular protein dynamics, which are dependent on external stimuli,  $\mathbf{u}_i$ , produced by connected cells. We define cellular connectivity in terms of multiple signaling mechanisms later in this section. Furthermore,  $\mathbf{h}: X \rightarrow Y$  describes the translation of intracellular dynamics to signal outputs of the cell. We assume that both functions  $\mathbf{f}(\cdot)$  and  $\mathbf{h}(\cdot)$  are  $\mathcal{C}^2$  over their respective domains to ensure the continuity of the corresponding linearized system that is required for the interconnected pattern analysis in section 3. The structure of the IO system (2.1) in the context of the tissue is shown in Figure 2. For convenience, when discussing tissue behavior, we define the large-scale vectorized counterparts of the intracellular state variables, signal inputs, and outputs by  $\mathbf{x} = [\mathbf{x}_1, \dots, \mathbf{x}_N]^T$ ,  $\mathbf{u} = [\mathbf{u}_1, \dots, \mathbf{u}_r]^T$ , and  $\mathbf{y} = [\mathbf{y}_1, \dots, \mathbf{y}_r]^T$ .

For the transition of signal outputs to inputs, we assume that each output signal is independent and defines a linear relationship between output and input signals. Let  $V := \{v_1, \dots, v_N\}$  be vertices representing the cells in the tissue. Then for each output signal  $y_{i,j}$ , there is an associated connectivity graph  $\mathcal{G}_j = \mathcal{G}_j(V, E_j)$ , where  $E_j$  is the set of edges for each output signal mechanism  $1 \leq j \leq r$ . Note that the vertex set  $V$  is identical for each connectivity graph, whereas edge structure may differ between the respective graphs to allow for different signaling mechanisms within the IO system (2.1). For example, the cellular connectivity graphs of contact-dependent and long-diffusion mechanisms have potentially different edge structures, as it is expected that the average degree of the contact-based graph is less than that of a diffusive mechanism due to the physical constraints of cellular junctions (Figure 2).

Algebraically, the cell-cell interaction graphs are represented using the weighted adjacency matrix,  $\mathbf{W}_j \in \mathbb{R}_{\geq 0}^{N \times N}$ . Let  $\mathcal{W} := \{\mathbf{W}_j\}$  be the set of weighted and row-stochastic adjacency matrices. That is, for any  $j \in \{1, \dots, r\}$  and any row  $i \in \{1, \dots, n\}$ , row-sum  $\sum_k (\mathbf{W}_j)_{ik} = 1$ , which represents the weighted average of signal transfer between connected cells. In addition, we assume that the connectivity graph  $\mathcal{G}_j$  associated with  $\mathbf{W}_j$  is undirected and connected, and thus  $\mathbf{W}_j$  is symmetric and irreducible; i.e., there exists no permutation matrix that transforms  $\mathbf{W}_j$  to upper triangular form [20]. We note that these assumptions are grounded in the underlying biological interactions that we model. Specifically, the undirected property of the graph can be justified by the symmetric signaling capacity that arises from the proximity-based juxtacrine and paracrine signaling mechanisms. Moreover, the cells represented by vertices in  $\mathcal{G}_j$  belong to a single tissue generating a connected structure.

To preserve the order of signal outputs,  $y_{i,j}$ , and therefore the cellular structure within the IO system (2.1), we construct a global interconnection matrix,  $\mathbf{P}$ , by interweaving each  $\mathbf{W}_j \in \mathcal{W}$  in order of output signal defined by  $y_{i,j}$ . Namely,

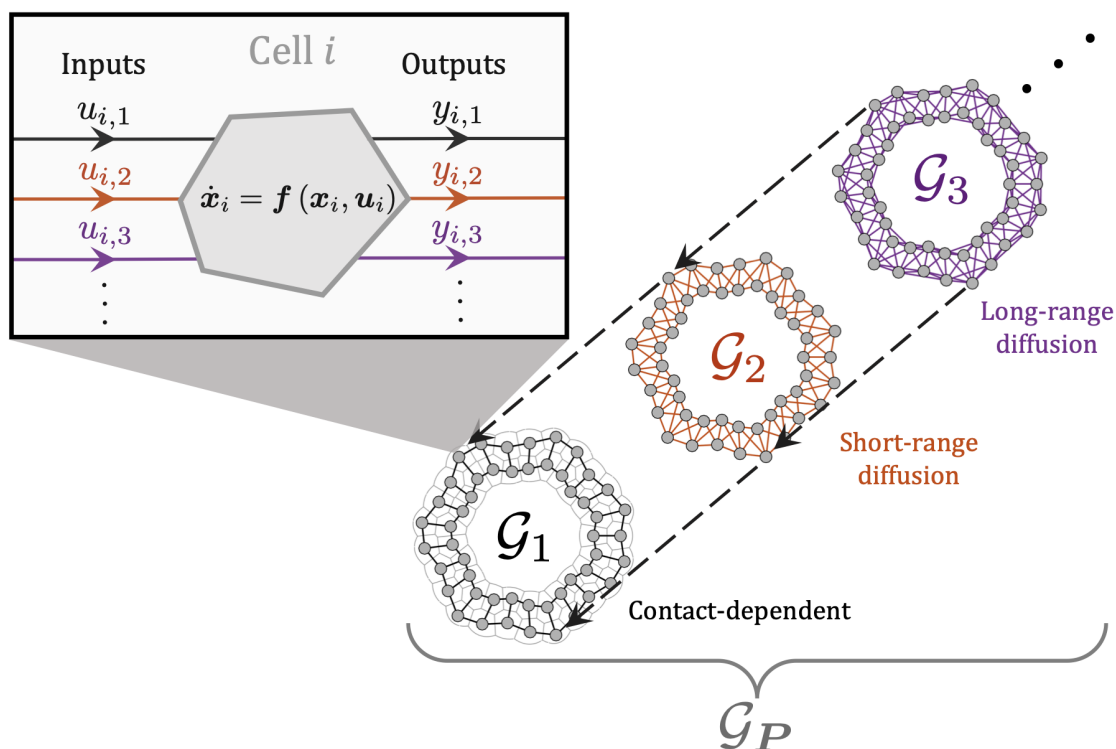


**Figure 2.** A graphical representation of the IO system (2.1) for bilayer geometries with multiple signaling mechanisms defined by the global adjacency matrix  $\mathbf{P}$  (2.3). Example two-dimensional bilayer graphs are shown for contact-dependent short- and long-range diffusion over the same vertex set representing the cells in the tissue, which are explicitly shown with membranes in  $\mathcal{G}_1$  to highlight the bilayer cellular structure. Each of the connectivity graphs is then embedded within the same vertex set as indicated by the dashed arrows. Therefore, each vertex contains the intracellular kinetics defined by the IO system (2.1), which responds to the signal outputs of adjacent cells for each signaling mechanism and is transformed to signal inputs by  $\mathbf{P}$  as defined in (2.5).

$$(2.3) \quad \mathbf{P} = \sum_{j=1}^r \mathbf{W}_j \otimes \mathbf{D}_j,$$

where  $\otimes$  is the Kronecker product and  $\mathbf{D}_j = \text{diag}(\delta_{j,1}, \dots, \delta_{j,r})$  for  $\delta_{i,j}$  the Kronecker delta function

$$(2.4) \quad \delta_{i,j} = \begin{cases} 1 & i = j, \\ 0 & i \neq j. \end{cases}$$

The global interconnection matrix  $\mathbf{P} \in \mathbb{R}^{rN \times rN}$  produces a multilayer graph  $\mathcal{G}_P$  that is layerwise independent, as shown in Figure 2. Critically, the construction of  $\mathbf{P}$  defines the linear relationship between global signal outputs and inputs,

$$(2.5) \quad \mathbf{u} = \mathbf{P}\mathbf{y},$$

where cellwise IO structure is preserved. The fundamental cellular identity preserving structure of  $\mathbf{P}$  is demonstrated in the following example.

*Example 2.1.* Consider the two general matrices

$$(2.6) \quad \mathbf{W}_1 = \begin{bmatrix} a_{11} & a_{12} \\ a_{21} & a_{22} \end{bmatrix} \quad \text{and} \quad \mathbf{W}_2 = \begin{bmatrix} b_{11} & b_{12} \\ b_{21} & b_{22} \end{bmatrix}$$

for the IO system (2.1) with only two cells each with two signal inputs and outputs, i.e.,  $r = 2$ . Then the global interconnection matrix,  $\mathbf{P}$ , has the form

$$(2.7) \quad \mathbf{P} = \begin{bmatrix} a_{11} & a_{12} \\ a_{21} & a_{22} \end{bmatrix} \otimes \begin{bmatrix} 1 & 0 \\ 0 & 0 \end{bmatrix} + \begin{bmatrix} b_{11} & b_{12} \\ b_{21} & b_{22} \end{bmatrix} \otimes \begin{bmatrix} 0 & 0 \\ 0 & 1 \end{bmatrix} = \begin{bmatrix} a_{11} & 0 & a_{12} & 0 \\ 0 & b_{11} & 0 & b_{12} \\ a_{21} & 0 & a_{22} & 0 \\ 0 & b_{21} & 0 & b_{22} \end{bmatrix}.$$

To study the role of layer-dependent signaling polarity for the generation of laminar patterns in bilayer geometries, we consider each graph to consist of two layers,  $\mathcal{L}_1 := \{v_1, \dots, v_{|\mathcal{L}_1|}\}$  and  $\mathcal{L}_2 := \{v_{|\mathcal{L}_1|+1}, \dots, v_N\}$ , where  $|\mathcal{L}_1| = 1, \dots, N - 1$ , as shown in Figures 2 and 3.

This layerwise grouping of the vertices also provides consistent structure to the weighted adjacency matrices  $\mathbf{W}_k \in \mathcal{W}$ . As a first approach to the layer-dependent signal polarity, we consider only two values of edge weights for connected cells in the same and different layers, as highlighted in Figure 3. Namely, consider the graph  $\mathcal{G}_k$  associated with  $\mathbf{W}_k$ . Then if  $v_i, v_j \in \mathcal{L}_1$  (or  $\mathcal{L}_2$ ) such that  $v_i$  and  $v_j$  are connected by an edge in  $\mathcal{G}_k$  and are in the same layer, then  $(\mathbf{W}_k)_{ij} = \hat{w}_1^{[k]}$  for  $\hat{w}_1^{[k]}$ , the row-normalized intralayer edge weight. Similarly, if  $v_i$  and  $v_j$  are in different layers,  $v_i \in \mathcal{L}_1$  and  $v_j \in \mathcal{L}_2$ , and are connected in  $\mathcal{G}_k$ , then  $(\mathbf{W}_k)_{ij} = \hat{w}_2^{[k]}$  for  $\hat{w}_2^{[k]}$ , the row-normalized interlayer edge weight. Consequently, when vertices are indexed consecutively from  $\mathcal{L}_1$  and then  $\mathcal{L}_2$ , each  $\mathbf{W}_k$  has block form

$$(2.8) \quad \mathbf{W}_k = \begin{bmatrix} \widehat{\mathbf{W}}_{1, \mathcal{L}_1}^{[k]} & \widehat{\mathbf{W}}_{2, \mathcal{L}_1}^{[k]} \\ \left(\widehat{\mathbf{W}}_{2, \mathcal{L}_1}^{[k]}\right)^T & \widehat{\mathbf{W}}_{1, \mathcal{L}_2}^{[k]} \end{bmatrix},$$

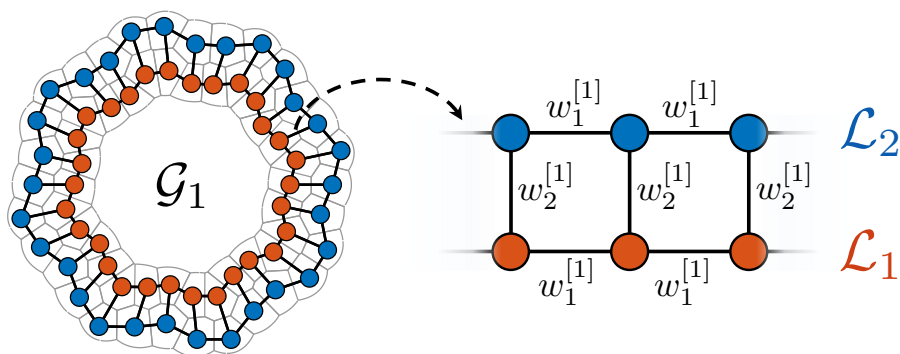


**Figure 3.** Layer-dependent edge weight structure in bilayer graphs. A two-dimensional bilayer graph,  $\mathcal{G}_1$ , with contact-dependent edge connections highlight the layer vertex partitions with vertices in  $\mathcal{L}_1$  and  $\mathcal{L}_2$ , colored orange and blue, respectively. The edge weight structure within and between the layers is shown with edges between vertices in the same layer weighted by  $w_1^{[1]}$  and connected vertices in different layers weighted by  $w_2^{[1]}$ .

where  $\widehat{\mathbf{W}}_{1,\mathcal{L}_1} \in \mathbb{R}_{\geq 0}^{|\mathcal{L}_1| \times |\mathcal{L}_1|}$  contains all intralayer connections scaled by  $\hat{w}_1^{[k]}$  for all the vertices in  $\mathcal{L}_1$  and  $\widehat{\mathbf{W}}_{2,\mathcal{L}_1} \in \mathbb{R}_{\geq 0}^{|\mathcal{L}_1| \times |\mathcal{L}_2|}$  contains all interlayer connections scaled by  $\hat{w}_2^{[k]}$  for all the vertices in  $\mathcal{L}_1$ . Similarly,  $\widehat{\mathbf{W}}_{1,\mathcal{L}_2} \in \mathbb{R}_{\geq 0}^{|\mathcal{L}_2| \times |\mathcal{L}_2|}$  accounts for the intralayer connections within  $\mathcal{L}_2$ . As each  $\mathcal{G}_k$  is undirected, the interlayer connections for all vertices in  $\mathcal{L}_2$  are represented by  $\widehat{\mathbf{W}}_{2,\mathcal{L}_1}^T$ ; that is,  $\mathbf{W}_k$  is symmetric.

*Example 2.2.* The weighted adjacency matrix  $\mathbf{W}_1$  associated with  $\mathcal{G}_1$  in Figure 3 has the block matrices

$$(2.9) \quad \widehat{\mathbf{W}}_{1,\mathcal{L}_1} = \begin{bmatrix} 0 & \hat{w}_1^{[1]} & 0 & \cdots & 0 & \hat{w}_1^{[1]} \\ \hat{w}_1^{[1]} & 0 & \hat{w}_1^{[1]} & & & \\ & & \ddots & & & \\ & & & \ddots & & \\ & & & & \hat{w}_1^{[1]} & 0 & \hat{w}_1^{[1]} \\ \hat{w}_1^{[1]} & 0 & \cdots & 0 & \hat{w}_1^{[1]} & 0 \end{bmatrix} \quad \text{and} \quad \widehat{\mathbf{W}}_{2,\mathcal{L}_1} = \begin{bmatrix} \hat{w}_2^{[1]} & 0 & 0 & \cdots & 0 & 0 \\ 0 & \hat{w}_2^{[1]} & 0 & & & \\ & & \ddots & & & \\ & & & \ddots & & \\ & & & & 0 & \hat{w}_2^{[1]} & 0 \\ 0 & 0 & \cdots & 0 & 0 & 0 & \hat{w}_2^{[1]} \end{bmatrix}$$

for  $\hat{w}_1^{[1]} = w_1^{[1]} / |w^{[1]}|$  and  $\hat{w}_2^{[1]} = w_2^{[1]} / |w^{[1]}|$ , where  $|w^{[1]}| = 2w_1^{[1]} + w_2^{[1]}$  is the normalizing factor for all rows ensuring the row-stochastic property of  $\mathbf{W}_1$ . From the regularity of  $\mathcal{G}_1$  in Figure 3, we have that  $\widehat{\mathbf{W}}_{1,\mathcal{L}_1} = \widehat{\mathbf{W}}_{1,\mathcal{L}_2}$ , as the connections within layers are identical for  $\mathcal{L}_1$  and  $\mathcal{L}_2$ .

To summarize the internal cellular dynamics in terms of signal inputs and outputs, as proposed in [7], we introduce the transfer function  $\mathbf{T} : U \rightarrow Y$ , which describes cellular signal output response with respect to changes to input signals determined by connected cells. It is assumed that  $\mathbf{T}(\cdot)$  is bounded and  $\mathcal{C}^2$ , which conforms with the biological context of the IO system (2.1); namely, intracellular expression must remain finite with continuous dependence on the cellular microenvironment. The introduction of  $\mathbf{T}(\cdot)$  allows for the analysis of the IO system (2.1) from an alternative macroscopic perspective such that  $\mathbf{T}(\cdot)$  retains the underlying features of the intracellular kinetics defined by  $\mathbf{f}(\cdot)$  and  $\mathbf{h}(\cdot)$  while not explicitly defining the intracellular interactions. For instance, intercellular communication of lateral-inhibition and lateral-induction pathways have a decreasing and increasing transfer function  $\mathbf{T}(\cdot)$ , respectively [7, 66]. Explicitly, the transfer function allows for the definition of the auxiliary input to output transition relation

$$(2.10) \quad \mathbf{u} = \mathbf{P}[\mathbf{T}(\mathbf{u}_1), \dots, \mathbf{T}(\mathbf{u}_N)]^T,$$

which reduces the analytic complexity of the macroscopic analysis of spatially driven pattern formation in large-scale systems, as the dependence of cellular coupling is more accessible in this form [7, 26, 52]. However, these methods require that the characteristic behavior of the GRNs is known with respect to intercellular signals, i.e., prescribing monotone properties for  $\mathbf{T}(\mathbf{u}_i)$ .

In the following section, we show that the zeros of the auxiliary input to output transition equation (2.10) are the steady states of the IO system (2.1), thus enabling stability analysis of the HSS macroscopically. Subsequently, we derive conditions for the existence and uniqueness

of the HSS in the large-scale system. To induce polarity-driven pattern formation within the IO system (2.1), we seek sufficient conditions for the instability of HSS dependent on the bilayer connectivity graphs  $\mathcal{G}_k$  and, in particular, the polarity weights  $w_1^{[k]}$  and  $w_2^{[k]}$ .

## 2.2. Existence, uniqueness, and stability of the HSS in the large-scale IO systems.

The majority of statements presented in this section were initially stated in [26] for MIMO IO systems. Here, we have independently proven them and partially extended them to comment on the uniqueness of the HSS. We include all results for completeness with a focus on the application to mixed signal mechanisms in bilayer geometries. Consider the  $\mathcal{C}^2$  function  $\mathbf{S} : U \rightarrow X$ , which describes the changes to the intracellular kinetics  $\mathbf{x}_i$  by the input signals  $\mathbf{u}_i$  emanating from connected cells. Therefore, the following statement demonstrates that the zeros of the auxiliary transfer relation (2.10) are the steady states of the IO system (2.1).

**Lemma 2.1** (see [25]). *Assume that for some  $\mathbf{u}_0 \in \mathbb{R}^r$ , the function  $\mathbf{f}(\mathbf{x}, \mathbf{u}_0) = 0$  has a solution denoted by  $\mathbf{x}_0 = \mathbf{S}(\mathbf{u}_0)$  and therefore that  $\mathbf{T}(\mathbf{u}_0) = \mathbf{h}(\mathbf{S}(\mathbf{u}_0))$ . If  $\mathbf{u}_0$  satisfies*

$$(2.11) \quad \begin{bmatrix} \mathbf{u}_0 \\ \vdots \\ \mathbf{u}_0 \end{bmatrix} = \mathbf{P} \begin{bmatrix} \mathbf{T}(\mathbf{u}_0) \\ \vdots \\ \mathbf{T}(\mathbf{u}_0) \end{bmatrix},$$

then  $\mathbf{x}_0 = \mathbf{S}(\mathbf{u}_0)$  is a steady state of the IO system (2.1). Conversely, if  $\mathbf{S}(\cdot)$  is injective and  $\mathbf{x}_0$  is a fixed point of the IO system (2.1), then the corresponding  $\mathbf{u}_0$  satisfies the auxiliary system (2.11).

Following from Lemma 2.1, we now study the transfer dynamics defined by  $\mathbf{T}(\cdot)$  for the existence of the steady states of the IO system (2.1). Critically, as  $\mathbf{T}(\cdot)$  represents changes in intercellular signaling,  $\mathbf{T}(\cdot)$  is bounded. Therefore, the following statement ensures the existence and uniqueness of an HSS of the IO system (2.1) using the boundedness of transfer dynamics.

**Lemma 2.2.** *Let  $\mathbf{u}_0 \in \mathbb{R}^r$  be such that the conditions of Lemma 2.1 hold and  $\mathbf{u}^* = \mathbf{1}_N \otimes \mathbf{u}_0$ . Then there exists  $\mathbf{x}_0 \in \mathbb{R}^n$  such that  $\mathbf{x}^* = \mathbf{1}_N \otimes \mathbf{x}_0$  is a steady state of the IO system (2.1). Moreover, if  $\partial \mathbf{f}(\mathbf{x}, \mathbf{u}_0) / \partial \mathbf{x}$  is invertible for all  $\mathbf{x} \in X$ , then  $\mathbf{x}^*$  is unique.*

*Proof.* It is sufficient to show that there exists  $\mathbf{u}_0 \in \mathbb{R}^r$  such that  $\mathbf{u}^* = \mathbf{1}_N \otimes \mathbf{u}_0$  satisfies the auxiliary system (2.11) as  $\mathbf{x}_0 = \mathbf{S}(\mathbf{u}_0)$ . As each  $\mathbf{W}_j \in \mathcal{W}$  is row-stochastic, the global interconnection matrix  $\mathbf{P}$  is also row-stochastic by construction. Consequently, there exists an eigenvalue  $\lambda$  of  $\mathbf{P}$  such that  $\mathbf{P}\mathbf{1}_{rN} = \lambda\mathbf{1}_{rN}$  [34], and therefore the proof follows from verifying the existence of  $\mathbf{u}_0$  that satisfies  $\mathbf{u}_0 = \lambda\mathbf{T}(\mathbf{u}_0)$ .

By the bounded property of  $\mathbf{T} : U \rightarrow Y$ , there exists some constant  $m > 0$ , where  $\|\lambda\mathbf{T}(\cdot)\|_2 \leq m$ . Consider the function  $\mathbf{F} : B_m \rightarrow B_m$ , where  $\mathbf{F}(\cdot) = \lambda\mathbf{T}(\cdot)$  and  $B_m = \{\mathbf{v} \in \mathbb{R}^r : \|\mathbf{v}\|_2 \leq m\}$ , noting that  $B_m$  is convex and that the continuity of  $\mathbf{F}(\cdot)$  is induced by the continuity of  $\mathbf{T}(\cdot)$ . Therefore, by the Brouwer fixed-point theorem [42], there exists some  $\mathbf{u}_0 \in B_m$  such that  $\mathbf{u}_0 = \mathbf{F}(\mathbf{u}_0) = \lambda\mathbf{T}(\mathbf{u}_0)$ .

The uniqueness of the HSS is guaranteed by the following. Assume that for any  $\mathbf{u}_0 \in \mathbb{R}^r$ , there exists  $\bar{\mathbf{x}}_1, \bar{\mathbf{x}}_2 \in \mathbb{R}^n$ , where both are solutions to  $\mathbf{f}(\mathbf{x}, \mathbf{u}_0) = \mathbf{0}$ . Specifically,  $f_j(\bar{\mathbf{x}}_1, \mathbf{u}_0) = f_j(\bar{\mathbf{x}}_2, \mathbf{u}_0)$  for all  $j \in \{1, \dots, n\}$ . Therefore, by the mean value theorem [40], we construct the linear system

$$(2.12) \quad \begin{bmatrix} 0 \\ \vdots \\ 0 \end{bmatrix} = \begin{bmatrix} \frac{\partial f_1}{\partial x_1}(\mathbf{x}, \mathbf{u}_0) & \cdots & \frac{\partial f_1}{\partial x_n}(\mathbf{x}, \mathbf{u}_0) \\ \vdots \\ \frac{\partial f_n}{\partial x_1}(\mathbf{x}, \mathbf{u}_0) & \cdots & \frac{\partial f_n}{\partial x_n}(\mathbf{x}, \mathbf{u}_0) \end{bmatrix} \begin{bmatrix} \bar{x}_{11} - \bar{x}_{21} \\ \vdots \\ \bar{x}_{1n} - \bar{x}_{2n} \end{bmatrix},$$

and from the invertible matrix theorem, the kernel of  $\partial \mathbf{f} / \partial \mathbf{x}$  contains only the null vector [35], i.e.,  $\bar{\mathbf{x}}_1 = \bar{\mathbf{x}}_2$ . ■

*Remark 2.1.* If the transfer function  $\mathbf{T} : U \rightarrow Y$  is Lipschitz continuous with Lipschitz constant  $k \in (0, 1]$ ,

$$(2.13) \quad \|\mathbf{T}(\mathbf{u}_i) - \mathbf{T}(\mathbf{u}_j)\|_2 \leq k \|\mathbf{u}_i - \mathbf{u}_j\|_2$$

for all  $\mathbf{u}_i, \mathbf{u}_j \in U$ . Then the HSS defined in Lemma 2.2 is unique by the Banach fixed-point theorem [1], independent of the invertibility of  $\mathbf{f}(\mathbf{x}, \mathbf{u})$ .

As we seek spatially driven instabilities of the HSS, we assume the asymptotic stability of  $\mathbf{x}^*$  in the absence of cellular connections. We say a fixed point of a system is stable if the associated Jacobian has all eigenvalues with negative real part. Therefore, we are assuming that  $\mathbf{A} := \partial \mathbf{f} / \partial \mathbf{x}_i$  evaluated at  $\mathbf{x}_0$  is stable; i.e., the intracellular kinetics are not self-exciting in the absence of interconnections.

A necessary feature for polarity-driven pattern formation in spatially discrete interconnected systems is the connectivity-induced instability of the HSS,  $\mathbf{x}^*$ , associated with the IO system (2.1), which can be approached by linearization. The following results provided a convenient method of analyzing the linear stability of homogeneous large-scale IO systems by assuming that each cellular connectivity graph  $\mathcal{G}_j$  commutes, thus enabling the parallel computation of eigenvalues for each adjacency matrix  $\mathbf{W}_j \in \mathcal{W}$ , reducing the dimensionality of the linearization.

*Lemma 2.3.* Let  $\mathbf{A} := \partial \mathbf{f} / \partial \mathbf{x}_i$ ,  $\mathbf{B} := \partial \mathbf{f} / \partial \mathbf{u}_i$ , and  $\mathbf{C} := \partial \mathbf{h} / \partial \mathbf{x}_i$  be each evaluated at the steady state  $\mathbf{x}_0$  for fixed  $\mathbf{u}_0$ . Let these steady state of the global IO system be  $\mathbf{x}^* = \mathbf{1}_N \otimes \mathbf{x}_0$ . Assume that all  $\mathbf{W}_j \in \mathcal{W}$  commute, and denote  $\mathbf{\Lambda}_j = \text{diag}(\lambda_{1,j}, \dots, \lambda_{r,j})$ , where  $\lambda_{i,j}$  is the  $j$ th eigenvalue of  $\mathbf{W}_i$  w.r.t. the common eigenbasis of all matrices in  $\mathcal{W}$ . Then  $\mathbf{x}^*$  is asymptotically stable if  $\mathbf{A} + \mathbf{B}\mathbf{\Lambda}_j\mathbf{C}$  is stable for all  $j$  and unstable otherwise.

*Proof.* Linearization of the global IO system (2.1) about the fixed point  $\mathbf{x}^* = \mathbf{I}_N \otimes \mathbf{x}_0$  yields the Jacobian

$$(2.14) \quad \begin{aligned} \mathbf{J} &= \mathbf{I}_N \otimes \mathbf{A} + (\mathbf{I}_N \otimes \mathbf{B}) \mathbf{P} (\mathbf{I}_N \otimes \mathbf{C}), \\ &= \mathbf{I}_N \otimes \mathbf{A} + (\mathbf{I}_N \otimes \mathbf{B}) \left( \sum_{i=1}^r \mathbf{W}_i \otimes \mathbf{D}_i \right) (\mathbf{I}_N \otimes \mathbf{C}), \\ &= \mathbf{I}_N \otimes \mathbf{A} + \sum_{i=1}^r \mathbf{W}_i \otimes \mathbf{B} \mathbf{D}_i \mathbf{C} \end{aligned}$$

by direct substitution of the definition of  $\mathbf{P}$  in terms of the independent signaling mechanisms and the mixed-product property of Kronecker products [27]. As  $\mathbf{W}_i \mathbf{W}_j = \mathbf{W}_j \mathbf{W}_i$  for

all  $\mathbf{W}_i, \mathbf{W}_j \in \mathcal{W}$  and all matrices  $\mathbf{W}_i$  are real and symmetric, there exists a matrix  $\mathbf{R}$  that simultaneously diagonalizes all adjacency matrices  $\mathbf{W}_i \in \mathcal{W}$  [35]. Moreover, the eigenbasis defined by  $\mathbf{R}$  fixes the order of the diagonal entries in each  $\mathbf{Z}_i = \mathbf{R}^{-1}\mathbf{W}_i\mathbf{R} = \text{diag}(\lambda_{i,1}, \dots, \lambda_{i,N})$  such that the sum of the diagonalized matrices  $\mathbf{Z}_i$  are unique. Specifically, reordering the eigenvectors that form the eigenbasis  $\mathbf{R}$  would only permute the sum of the diagonal values of  $\mathbf{Z}_i$ .

Consider the transformed Jacobian  $\mathbf{H} = (\mathbf{R}^{-1} \otimes \mathbf{I}_n) \mathbf{J} (\mathbf{R} \otimes \mathbf{I}_n)$ . Then by the mixed-product property of Kronecker products,

$$\begin{aligned} \mathbf{H} &= (\mathbf{R}^{-1} \otimes \mathbf{I}_n) (\mathbf{I}_N \otimes \mathbf{A}) (\mathbf{R} \otimes \mathbf{I}_n) + (\mathbf{R}^{-1} \otimes \mathbf{I}_n) \left( \sum_{i=1}^r \mathbf{W}_i \otimes \mathbf{B} \mathbf{D}_i \mathbf{C} \right) (\mathbf{R} \otimes \mathbf{I}_n), \\ &= \mathbf{R}^{-1} \mathbf{I}_N \mathbf{R} \otimes \mathbf{I}_n \mathbf{A} \mathbf{I}_n + \sum_{i=1}^r \mathbf{R}^{-1} \mathbf{W}_i \mathbf{R} \otimes \mathbf{I}_n \mathbf{B} \mathbf{D}_i \mathbf{C} \mathbf{I}_n, \\ (2.15) \quad &= \mathbf{I}_N \otimes \mathbf{A} + \sum_{i=1}^r \mathbf{Z}_i \otimes \mathbf{B} \mathbf{D}_i \mathbf{C}. \end{aligned}$$

By the diagonal structure of  $\mathbf{Z}_i$ , the matrix  $\mathbf{H}$  has the block diagonal form

$$(2.16) \quad \mathbf{H} = \begin{bmatrix} \mathbf{A} + \sum_{i=1}^r \lambda_{i,1} \mathbf{B} \mathbf{D}_i \mathbf{C} & & \\ & \ddots & \\ & & \mathbf{A} + \sum_{i=1}^r \lambda_{i,n} \mathbf{B} \mathbf{D}_i \mathbf{C} \end{bmatrix},$$

and therefore, as  $\sum_{i=1}^r \lambda_{i,j} \mathbf{B} \mathbf{D}_i \mathbf{C} = \mathbf{B} \mathbf{\Lambda}_j \mathbf{C}$ , the eigenvalues of  $\mathbf{H}$  are those of  $\mathbf{A} + \mathbf{B} \mathbf{\Lambda}_j \mathbf{C}$  for all  $1 \leq j \leq N$ . Consequently, if  $\mathbf{A} + \mathbf{B} \mathbf{\Lambda}_j \mathbf{C}$  has eigenvalues with all negative real part, for all  $1 \leq j \leq N$ , then  $\mathbf{H}$  is stable, and therefore the stability of  $\mathbf{J}$  follows by the bijection between the linearized systems  $\mathbf{H}$  and  $\mathbf{J}$ . ■

Before discussing the behavior of flows of the IO system (2.1) near the HSS, we first introduce a convenient condition for the instability of a matrix.

**Lemma 2.4** (see [52]). *If  $\mathbf{M} \in \mathbb{R}^{n \times n}$  is stable, then  $(-1)^n \det(\mathbf{M}) > 0$ . Conversely, if  $(-1)^n \det(\mathbf{M}) < 0$ , then  $\mathbf{M}$  has an eigenvalue with positive real part.*

Invoking Lemmas 2.3 and 2.4 leads to the following sufficient condition for the instability of the HSS associated with an IO system (2.1) with commuting connectivity graphs  $\mathcal{G}_j$ .

**Theorem 2.5.** *Consider the large-scale IO system (2.1), which is spatially coupled via the global interconnection matrix  $\mathbf{P}$  (2.3) such that each  $\mathbf{W}_j \in \mathcal{W}$  commutes. Denote  $\mathcal{DT} := \partial \mathbf{T} / \partial \mathbf{u}_i$ , and let  $\mathbf{\Lambda}_j = \text{diag}(\lambda_{1,j}, \dots, \lambda_{r,j})$ , where  $\lambda_{i,j}$  is the  $j$ th eigenvalue of  $\mathbf{W}_i$  w.r.t. the common eigenbasis of all matrices in  $\mathcal{W}$ . Then the HSS  $\mathbf{x}^* = \mathbf{1}_N \otimes \mathbf{x}_0$  is unstable if there exists a  $\mathbf{\Lambda}_j$  such that*

$$(2.17) \quad \prod_{i=1}^r (1 - \mu_{i,j}) < 0,$$

where  $\mu_{i,j}$  are the eigenvalues of  $\mathbf{\Lambda}_j \mathcal{DT}(\mathbf{u}_0)$  and  $\mathbf{u}_0$  is the steady-state input vector associated with  $\mathbf{x}_0$ .

*Proof.* By Lemma 2.3, we only need to show that there exists a positive eigenvalue of  $\mathbf{A} + \mathbf{B}\mathbf{\Lambda}_j\mathbf{C}$  for  $\mathbf{\Lambda}_j$  some diagonal matrix of eigenvalues of all matrices  $\mathbf{W}_i \in \mathcal{W}$  to demonstrate the instability of the HSS. Consider  $(-1)^n \det(\mathbf{A} + \mathbf{B}\mathbf{\Lambda}_j\mathbf{C})$ . Then by Sylvester’s determinant theorem [69], we have that

$$(2.18) \quad \begin{aligned} (-1)^n \det(\mathbf{A} + \mathbf{B}\mathbf{\Lambda}_j\mathbf{C}) &= (-1)^n \det(\mathbf{A}) \det(\mathbf{I}_r + \mathbf{\Lambda}_j\mathbf{C}\mathbf{A}^{-1}\mathbf{B}), \\ &= (-1)^n \det(\mathbf{A}) \det(\mathbf{I}_r - \mathbf{\Lambda}_j\mathcal{DT}(\mathbf{u}_0)), \end{aligned}$$

where the final equality holds from  $\mathcal{DT}(\mathbf{u}_0) = -\mathbf{C}\mathbf{A}^{-1}\mathbf{B}$  as derived in [7]. As  $\mathbf{A}$  is stable by assumption, we have that  $\mathbf{A}^{-1}$  exists and  $(-1)^n \det(\mathbf{A}) > 0$  by Lemma 2.4. Therefore, if  $\det(\mathbf{I}_r - \mathbf{\Lambda}_j\mathcal{DT}(\mathbf{u}_0)) < 0$ , then  $\mathbf{x}^* = \mathbf{1}_N \otimes \mathbf{x}_0$  is unstable by the converse statement of Lemma 2.4. Hence, as the determinant of a matrix is the product of the eigenvalues [35], we have that

$$(2.19) \quad \det(\mathbf{I}_r - \mathbf{\Lambda}_j\mathcal{DT}(\mathbf{u}_0)) = \prod_{i=1}^r (1 - \mu_{i,j})$$

for all matrices  $\mathbf{\Lambda}_j$  ( $1 \leq j \leq N$ ). ■

Applying the HSS instability condition derived in Theorem 2.5, IO systems with one or two spatially dependent components, known as single-input and single-output (SISO) and double-input and double-output (DIDO) interconnected systems, produce simple forms of the instability condition (2.17). Explicitly, the IO system (2.1) is SISO when  $r = 1$  and DIDO when  $r = 2$ . Let  $\text{Spec}(\mathbf{M})$  denote the set of eigenvalues of  $\mathbf{M}$ . Then, critically, we recover the SISO instability condition initially derived in [7], where we allow for generic intracellular kinetics here.

**Corollary 2.6.** *Consider the large-scale IO system (2.1), and denote  $\mathcal{DT} := \partial\mathbf{T}/\partial\mathbf{u}_i$ . We have the following:*

- (i) *If the IO system (2.1) is SISO with connectivity matrix  $\mathbf{W}_1$ , then the HSS  $\mathbf{x}^* = \mathbf{1}_N \otimes \mathbf{x}$  is unstable if*

$$(2.20) \quad 1 < \lambda_{1,j}T'(u_0)$$

for some  $\lambda_{1,j} \in \text{Spec}(\mathbf{W}_1)$ .

- (ii) *If the IO system (2.1) is DIDO with global interconnection matrix  $\mathbf{P}$  constructed by the commutative adjacency matrices  $\mathbf{W}_1$  and  $\mathbf{W}_2$ , then the HSS  $\mathbf{x}^* = \mathbf{1}_N \otimes \mathbf{x}$  is unstable if*

$$(2.21) \quad 1 < \text{tr}(\mathbf{\Lambda}_j\mathcal{DT}(\mathbf{u}_0)) - \det(\mathbf{\Lambda}_j\mathcal{DT}(\mathbf{u}_0))$$

for some  $\mathbf{\Lambda}_j = \text{diag}(\lambda_{1,j}, \lambda_{2,j})$ , where  $\lambda_{1,j} \in \text{Spec}(\mathbf{W}_1)$  and  $\lambda_{2,j} \in \text{Spec}(\mathbf{W}_2)$  are both associated with the same eigenvector.

*Proof.* In the case of a SISO system when  $r = 1$ , the  $T : U \rightarrow V$  is a scalar function, and we have that inequality (2.17) simply becomes  $1 - \lambda_{1,j}T'(u_0) < 0$ , yielding the SISO condition (2.20). For a DIDO system where  $r = 2$ , there are two potentially different adjacency matrices  $\mathbf{W}_1$  and  $\mathbf{W}_2$  that form  $\mathbf{P}$ . Therefore, from inequality (2.17), we have that

$$(2.22) \quad \begin{aligned} 0 > (1 - \mu_1)(1 - \mu_2) &= 1 + \text{tr}(-\mathbf{\Lambda}_j\mathcal{DT}(\mathbf{u}_0)) + \det(-\mathbf{\Lambda}_j\mathcal{DT}(\mathbf{u}_0)) \\ &= 1 - \text{tr}(\mathbf{\Lambda}_j\mathcal{DT}(\mathbf{u}_0)) + \det(\mathbf{\Lambda}_j\mathcal{DT}(\mathbf{u}_0)) \end{aligned}$$

using the relations between determinant, trace, and the eigenvalues of a matrix [35]. Rearrangement of inequality (2.22) yields the DIDO HSS instability condition (2.21). ■

The HSS instability conditions outlined in Theorem 2.5 allow the study of polarity regimes via graph edge weights to induce heterogeneity of cellular states within the bilayer tissues using analytic methods. Critically, the sufficient patterning conditions of Theorem 2.5 are independent of the precise intracellular kinetics, and we do not impose any specific feature on the transfer function,  $\mathbf{T}(\cdot)$  other than the mild requirement of boundedness that follows immediately when modeling protein dynamics.

In the following section, we introduce methods of graph partitioning for templating laminar patterns in bilayer geometries that produce analytic conditions for the existence of the laminar patterns with multiple signaling mechanisms. Formally, we define laminar patterns in bilayer graphs in the following way.

**Definition 2.1 (laminar patterns in bilayer IO systems).** *Let  $\mathbf{x}_+$  and  $\mathbf{x}_-$  be heterogeneous steady states of the IO system (2.1), i.e.,  $\mathbf{x}_+, \mathbf{x}_- \in X$  and  $\mathbf{x}_- \neq \mathbf{x}_+$ . The IO system (2.1) is said to have converged to a laminar pattern state if for some  $t_0 > 0$ , we have  $\mathbf{x}_i = \mathbf{x}_-$  and  $\mathbf{x}_j = \mathbf{x}_+$  for  $i = 1, \dots, |\mathcal{L}_1|$  and  $j = |\mathcal{L}_1| + 1, \dots, N$  and for all  $t > t_0$ .*

When seeking laminar pattern formation in the bilayer IO system (2.1), we show that the commutative properties of the adjacency matrices  $\mathbf{W}_j \in \mathcal{W}$  required for the HSS instability condition in Theorem 2.5 can be relaxed when seeking dichotomous cell states in bilayer structures with the same layer of connectivity symmetries, namely, semiregular bilayer graphs. In addition, by restricting the characteristic behavior of intracellular kinetics to competitive interactions, we ensure that the HSS instability converges to laminar patterns by applying results from monotone dynamical system theory.

### 3. Laminar pattern convergence with monotone kinetics in semiregular bilayer graphs.

The instability of the HSS of the IO system (2.1) does not imply the existence of stable heterogeneous cell states, even in systems with a unique HSS and bounded dynamics, as there may exist oscillatory or chaotic solution trajectories. We leverage results from monotone dynamic systems and techniques of graph symmetry reduction to ensure the convergence to dichotomous cell states at the instance of HSS instability in the bilayer geometries. These methods of discrete pattern analysis were first introduced for SISO systems in [52] and later briefly extended to MIMO systems in [26]. Here we demonstrate the applicability of these methods to two-state pattern formation with pathway crosstalk kinetics in bilayer geometries. In addition, we emphasize the link to the corresponding large-scale IO system (2.1); namely, when are the predicted patterns in the symmetry-reduced system preserved in the large-scale system?

**3.1. Monotone kinetics for pattern convergence.** Let  $\phi_t(\mathbf{x}_1)$  and  $\phi_t(\mathbf{x}_2)$  be two solutions to the IO system (2.1), where  $\mathbf{x}_1 \leq \mathbf{x}_2$  are initial conditions. It is said that the dynamical system (2.1) is monotone if  $\phi_t(\mathbf{x}_1) \leq \phi_t(\mathbf{x}_2)$  for all  $t \in [0, \infty)$  [57]. Furthermore, the IO system (2.1) is said to be strongly monotone if  $\phi_t(\mathbf{x}_1) < \phi_t(\mathbf{x}_2)$  for all  $t \in [0, \infty)$  [57]. Critically, the property of strong monotonicity is crucial for the asymptotic convergence of solutions  $\phi_t(\mathbf{x})$  on bounded domains  $X \subset \mathbb{R}_{\geq 0}^n$ , analogous to the monotone convergence theorem for bounded sequences [31].

A dynamical system can be shown to be monotone by studying the sign structure of the associated Jacobian matrix on convex domains. The trajectory domain  $X$  is convex if for any  $\mathbf{a}, \mathbf{b} \in X$ ,  $t\mathbf{a} + (1 - t)\mathbf{b} \in X$  for all  $t \in [0, 1]$ ; i.e., there exists a line segment between any two points in the domain that lies in the interior of  $X$ . The monotone identification via the Jacobian matrix relies on the intercomponent monotonicity of vector-valued functions and the convexity of their respective domains, as initially studied by Kamke [36], leading to the classification of type K functions. Namely, a function  $\mathbf{g}(\cdot)$  is said to be type K if for each  $i$ ,  $g_i(\mathbf{a}) \leq g_i(\mathbf{b})$  for any two points  $\mathbf{a}, \mathbf{b} \in X$  satisfying  $\mathbf{a} \leq \mathbf{b}$  and  $a_i = b_i$ , where  $X$  is a convex domain [57]. The identification of type K functions in dynamical systems leads to the sufficient condition for monotone trajectories.

**Lemma 3.1 (type K monotone systems [57]).** *Consider the general autonomous dynamical system*

$$(3.1) \quad \dot{\mathbf{z}} = \mathbf{g}(\mathbf{z}),$$

where  $\mathbf{z} \in Z$  and  $Z \subset \mathbb{R}^n$  is convex. Then the dynamical system (3.1) is monotone if it is type K. Furthermore, by the fundamental theorem of calculus, the general autonomous dynamical system (3.1) is guaranteed to be type K when the row-sums of the associated Jacobian satisfy

$$(3.2) \quad \sum_{j \neq i} \frac{\partial g_i}{\partial z_j} \geq 0$$

for all  $1 \leq i \leq n$ .

A direct consequence of Lemma 3.1 is that the IO system (2.1) is monotone provided that all off-diagonal components of the associated Jacobian are nonnegative for all  $\mathbf{x} \in X$  as previously applied in large-scale IO pattern formation studies [7, 25]. In addition, Hirsch provided a sufficient condition for strong monotonicity that is dependent on the irreducibility of the Jacobian of the dynamical system [28]. Specifically, a matrix  $\mathbf{M}$  is said to be irreducible if there exists no permutation matrix  $\mathbf{U}$  such that  $\mathbf{U}^T \mathbf{M} \mathbf{U}$  is in upper block triangular form [69].

**Lemma 3.2 (see [57]).** *Consider the dynamical system (3.1) as in Lemma 3.1. If the Jacobian,  $\frac{\partial \mathbf{g}}{\partial \mathbf{z}}$ , is irreducible and type K for all  $\mathbf{z} \in Z$ , then system (3.1) is strongly monotone.*

The combination of Lemmas 3.1 and 3.2 yields sufficient conditions for the identification of strongly monotone dynamical systems using standard linearization methods, which are particularly applicable to interconnected dynamical systems. Namely, connected graphs have irreducible adjacency matrices [20].

Time-dependent monotone systems are often characterized into two distinctive classes: cooperative dynamics, where all solutions are monotone in forward time ( $t \rightarrow \infty$ ), and competitive dynamics, where all solutions are monotone in backward time ( $t \rightarrow -\infty$ ) [57]. It has previously been demonstrated that competitive dynamics lead to pattern generation in large-scale IO systems, specifically when studying processes of mutual cellular inhibition, which are a common feature of cell-fate dynamics in developing tissues [7]. For example, the lateral-inhibition interactions of Notch1 and Delta1 are often found in tissues with a dichotomy of

spatially organized cell types and conform to the monotone competitive description [16, 44]. Subsequently, we focus our attention on competitive intracellular kinetics, which leads to the following assumption on the behavior of the transfer function  $\mathbf{T}(\cdot)$  to ensure the asymptotic convergence of solutions with tissue heterogeneity:

- (A1) The derivative of the transfer function  $\mathcal{DT}(\mathbf{u})$  of the IO system (2.1) has one of the sign structures

$$\mathcal{S}_1 = \begin{bmatrix} - & + & \cdots & - & + \\ + & - & \cdots & + & - \\ & & \vdots & & \\ - & + & \cdots & - & + \\ + & - & \cdots & + & - \end{bmatrix} \quad \mathcal{S}_2 = \begin{bmatrix} - & - & \cdots & - & - \\ - & - & \cdots & - & - \\ & & \vdots & & \\ - & - & \cdots & - & - \\ - & - & \cdots & - & - \end{bmatrix}$$

for all  $\mathbf{u} \in U$ , where any sign can be replaced by zero provided  $\mathcal{DT}(\mathbf{u})$  is irreducible. Critically, the conditions imposed on the intracellular kinetics by (A1) are not restrictive in the context of cellular pattern formation, as activation and repression of intracellular signals are typically modeled using monotonic functions, such as Hill or logistic functions that relate to Michaelis–Menten kinetics for enzyme-catalyst reactions [38]. Furthermore, the irreducibility of  $\mathcal{DT}(\mathbf{u})$  follows immediately if there exist no zero entries. That is, each spatially dependent component is continuously dependent on all other spatially dependent components.

In the following section, we will use the competitive properties of the transfer function to predict the existence of laminar pattern formation in bilayer geometry graph partitioning. In particular, we focus on the analysis of the transfer function, as this considers only the spatially dependent components of the IO system (2.1), which potentially reduces the dimensionality of the analysis while preserving the underlying behavior of the system.

### 3.2. Dimension reduction by graph partition for polarity laminar pattern existence.

Methods of graph partitioning have previously been employed in large-scale IO systems to predict the existence of patterns with a predefined pattern structure [25, 52]. These predefined pattern structures allow for the construction of bespoke systems by exploiting the symmetries of the cellular connectivity graphs,  $\mathcal{G}_k$ , thereby analyzing only representative vertices from each pattern partition of the large-scale graphs and vastly reducing the dimensionality-associated IO systems. Under the assumption of monotone transfer kinetics (A1), we provide sufficient conditions for the existence of polarity-driven laminar patterns in bilayer geometries with multiple spatially dependent components using graph partitioning. Critically, we demonstrate that the prior requirement of commutative connectivity graphs  $\mathcal{G}_j$  can be relaxed when seeking patterns with only two contrasting states.

The method of pattern templating via graph partitions seeks to group cells that are assumed to have the same steady-state solutions and therefore impose that cells within the same group behave identically, more formally described as synchronized vertex dynamics [2, 3, 59]. This assumption allows for the study of two representative cells from each layer in the bilayer large-scale graphs,  $\mathcal{G}_k$ , to predict the existence of laminar patterns, as shown in Figure 4. Formally, we are assuming the existence of an equitable partition,  $\pi_2$ , of the vertices  $v_i \in V$  into the pattern groups  $\mathcal{L}_1$  and  $\mathcal{L}_2$  of each layer for all connectivity graphs  $\mathcal{G}_k$ . This means that  $v \in \mathcal{L}_i$  has the same number of adjacent vertices in both  $\mathcal{L}_1$  and  $\mathcal{L}_2$ , independent of the

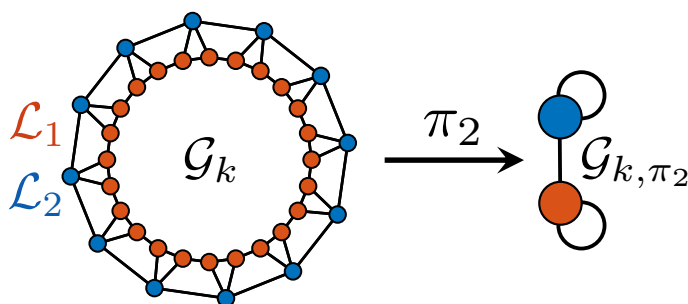


**Figure 4.** Templating for laminar patterns in bilayer geometries using the equitable partition  $\pi_2$ . The cellular connectivity graph,  $\mathcal{G}_k$ , is semiregular. Such vertices within the same layer,  $\mathcal{L}_1$  or  $\mathcal{L}_2$ , have the same number of adjacent vertices in each of the layers, which induce an edge symmetry with respect to vertices in the same layer. The equitable partition,  $\pi_2$ , leverages the edge symmetries of  $\mathcal{G}_k$  to generate a quotient graph  $\mathcal{G}_{k,\pi_2}$  consisting of two representative cells, one from each layer  $\mathcal{L}_1$  and  $\mathcal{L}_2$ .

vertex,  $v$  [20]. We are imposing that cells within the same layer have the same edge connectivity structure, and therefore the connectivity graphs  $\mathcal{G}_k$  must be layerwise regular, as highlighted in Figure 4. However, we note that these connectivity symmetries are not necessary for the construction of an equitable partition with weighted edges [2]. Algebraically, the partition  $\pi_2$  is equitable if there exists some  $\bar{w}_{ij}^{[k]} > 0$  such that

$$(3.3) \quad \sum_{v \in \mathcal{L}_j} \hat{w}_{uv}^{[k]} = \bar{w}_{ij}^{[k]} \quad \forall u \in \mathcal{L}_i,$$

where  $\hat{w}_{ij}^{[k]}$  are the  $ij$ th elements of the row-stochastic adjacency matrix  $\mathbf{W}_k \in \mathcal{W}$  [20]. In addition, we say that the laminar pattern partition,  $\pi_2$ , is simultaneously equitable if  $\pi_2$  is equitable for all graphs  $\mathcal{G}_k$ .

Let  $\bar{\mathbf{W}}_k \in \mathbb{R}_{\geq 0}^{2 \times 2}$  be the reduced adjacency matrix for the quotient graph  $\mathcal{G}_{k,\pi_2} = \mathcal{G}_k/\pi_2$ , as depicted in Figure 4, that are elementwise composed with the constants defined by (3.3). Applying the IO-preserving interconnection matrix definition (2.3) to the set of reduced adjacency matrices, we have the reduced interconnection matrix of the form

$$(3.4) \quad \bar{\mathbf{P}} = \sum_{i=1}^r \bar{\mathbf{W}}_i \otimes \mathbf{D}_i,$$

noting that the row-stochastic property of each  $\mathbf{W}_i \in \mathcal{W}$  is preserved in the quotient mapping such that each  $\bar{\mathbf{W}}_i$  is row-stochastic. In particular, as the partition  $\pi_2$  allocates the vertices  $v \in V$  into either of the sets,  $\mathcal{L}_1$  or  $\mathcal{L}_2$ , each reduced adjacency matrix is of the form

$$(3.5) \quad \bar{\mathbf{W}}_i = \begin{bmatrix} a_i & 1 - a_i \\ 1 - b_i & b_i \end{bmatrix}$$

for all  $1 \leq i \leq r$ , where  $a_i, b_i \in (0, 1)$  are composed of the polarity weights  $w_1^{[i]}$  and  $w_2^{[i]}$ . Explicitly,  $a_i$  and  $b_i$  have the layer-dependent form

$$(3.6) \quad a_i = \frac{n_{1,\mathcal{L}_1}^{[i]} w_1^{[i]}}{n_{1,\mathcal{L}_1}^{[i]} w_1^{[i]} + n_{2,\mathcal{L}_1}^{[i]} w_2^{[i]}} \quad \text{and} \quad b_i = \frac{n_{1,\mathcal{L}_2}^{[i]} w_1^{[i]}}{n_{1,\mathcal{L}_2}^{[i]} w_1^{[i]} + n_{2,\mathcal{L}_2}^{[i]} w_2^{[i]}}$$

where the superscripts correspond to the spatial connectivity mechanism,  $i$ , and  $n_{1,\mathcal{L}_j}^{[i]} \geq 1$  and  $n_{2,\mathcal{L}_j}^{[i]} \geq 1$  are the number of connected vertices in the same and opposing layers, respectively, from the perspective of each layer,  $j = 1, 2$ . For example,  $n_{1,\mathcal{L}_1}^{[k]} = n_{1,\mathcal{L}_2}^{[k]} = 2$ ,  $n_{2,\mathcal{L}_1}^{[k]} = 1$ , and  $n_{2,\mathcal{L}_2}^{[k]} = 2$  for  $\mathcal{G}_k$  in Figure 4.

A key property of the equitable partition,  $\pi_2$ , is the preservation of eigenvalues when mapping between the large-scale and quotient graphs, that is,  $\text{Spec}(\overline{\mathbf{W}}_i) \subset \text{Spec}(\mathbf{W}_i)$  [20]. Using this property, any spatially driven instability of the HSS observed in the quotient system also exists in the associated large-scale system. However, to apply the HSS instability conditions derived in Theorem 2.5 to large-scale connectivity graphs, we require that all  $\overline{\mathbf{W}}_i$  commute to generate a common eigenbasis for simultaneous diagonalization. Commutativity is not preserved in the quotient transformation in general due to the reduced form of (3.5), although the following statement enables the use of the HSS instability conditions independent of the commutative properties of  $\overline{\mathbf{W}}_i$  by demonstrating the existence of a common eigenbasis for all reduced adjacency matrices partitioned by  $\pi_2$ , independent of commutativity.

**Lemma 3.3.** *Let  $\overline{\mathbf{P}} \in \mathbb{R}_{\geq 0}^{2r \times 2r}$  be the reduced mixed interconnection matrix equation (3.4) associated with the equitable partition  $\pi_2$ . Given any matrix  $\widetilde{\mathbf{M}} \in \mathbb{R}^{r \times r}$ , where  $\mathbf{M} = \mathbf{I}_2 \otimes \widetilde{\mathbf{M}}$ , the eigenvalues of  $\overline{\mathbf{P}}\mathbf{M}$  are those of  $\widetilde{\mathbf{M}}$  and  $\overline{\Lambda}_2\widetilde{\mathbf{M}}$ , where  $\overline{\Lambda}_2 = \text{diag}(a_1 + b_1 - 1, \dots, a_r + b_r - 1)$ .*

*Proof.* By definition of the family of the reduced adjacency matrices equation (3.5),  $\text{Spec}(\overline{\mathbf{W}}_i) = \{1, a_i + b_i - 1\}$ , where all reduced adjacency matrices share the common eigenvector  $\mathbf{v}_1 = \mathbf{1}_2$ , associated with the common eigenvalue  $\lambda_{i,1} = 1$ . Without loss of generality, let  $\widetilde{\mathbf{R}}$  be the transformation matrix for  $\overline{\mathbf{W}}_1$  such that  $\widetilde{\mathbf{R}}^{-1}\overline{\mathbf{W}}_1\widetilde{\mathbf{R}}$  is in Jordan normal form [35]. Specifically, as  $\mathbf{v}_1$  must represent a column of  $\widetilde{\mathbf{R}}$ , as it is an eigenvector for all  $\overline{\mathbf{W}}_i$ , let  $\mathbf{v}_1$  form the first column of  $\widetilde{\mathbf{R}}$  such that  $\widetilde{\mathbf{R}}^{-1}\overline{\mathbf{W}}_1\widetilde{\mathbf{R}}$  has diagonal entries 1 and  $a_1 + b_1 - 1$ , respectively. Moreover, as each  $\overline{\mathbf{W}}_i \in \mathbb{R}_{\geq 0}^{2 \times 2}$ ,  $\widetilde{\mathbf{R}}^{-1}\overline{\mathbf{W}}_i\widetilde{\mathbf{R}}$  must be in upper triangular form, as 1 is a common eigenvalue for all  $1 \leq i \leq r$ ; that is,  $\widetilde{\mathbf{R}}$  simultaneously upper triangularizes the family of reduced adjacency matrices such that each  $\widetilde{\mathbf{R}}^{-1}\overline{\mathbf{W}}_i\widetilde{\mathbf{R}}$  has diagonal entries 1 and  $a_i + b_i - 1$ .

Consider the invertible transformation  $\mathbf{R} = \widetilde{\mathbf{R}} \otimes \mathbf{I}_r$ . Denote the adjacency triangulation transformation of  $\overline{\mathbf{P}}\mathbf{M}$  by  $\mathbf{H} = \mathbf{R}^{-1}\overline{\mathbf{P}}\mathbf{M}\mathbf{R}$ . Therefore, we have that

$$\begin{aligned} \mathbf{H} &= \left(\widetilde{\mathbf{R}}^{-1} \otimes \mathbf{I}_r\right) \overline{\mathbf{P}}\mathbf{M} \left(\widetilde{\mathbf{R}} \otimes \mathbf{I}_r\right), \\ &= \left(\widetilde{\mathbf{R}}^{-1} \otimes \mathbf{I}_r\right) \left(\sum_{i=1}^r \overline{\mathbf{W}}_i \otimes \mathbf{D}_i\right) \left(\mathbf{I}_2 \otimes \widetilde{\mathbf{M}}\right) \left(\widetilde{\mathbf{R}} \otimes \mathbf{I}_r\right), \\ (3.7) \quad &= \sum_{i=1}^r \widetilde{\mathbf{R}}^{-1} \overline{\mathbf{W}}_i \widetilde{\mathbf{R}} \otimes \mathbf{D}_i \widetilde{\mathbf{M}}. \end{aligned}$$

Specifically,  $\mathbf{H}$  is of block upper triangle form such that

$$(3.8) \quad \mathbf{H} = \begin{bmatrix} \mathbf{I}_r \widetilde{\mathbf{M}} & \mathbf{Z} \widetilde{\mathbf{M}} \\ \mathbf{0} & \overline{\Lambda}_2 \widetilde{\mathbf{M}} \end{bmatrix},$$

where  $\mathbf{Z}$  is some real  $r \times r$  matrix constructed by interweaving the upper right entries of the transformed reduced adjacency matrices. Thus, the eigenvalues of  $\mathbf{H}$  are those of  $\widetilde{\mathbf{M}}$  and  $\overline{\Lambda}_2 \widetilde{\mathbf{M}}$  and therefore are the eigenvalues of  $\overline{\mathbf{P}}\mathbf{M}$  via bijective transformation defined by  $\mathbf{R}$ . ■

Subsequently, by seeking the existence of laminar patterns using the partition  $\pi_2$ , Lemma 3.3 enables an analytic approach to determine the spatially driven instability of the HSS with any combination of layerwise semiregular bilayer graphs. Specifically, we need only determine the eigenvalues of  $\mathcal{DT}(\mathbf{u}^*)$  to ensure that the HSS instability condition (2.17) is satisfied.

By applying the strongly monotone properties of the transfer kinetics outlined in section 3.1, we seek to ensure the asymptotic convergence of heterogeneous solutions in the instance of HSS instability. However, it can be shown (see Lemma A.1 in Appendix A) that the interconnection matrix,  $\mathbf{P}$ , and consequently the reduced interconnection matrix  $\overline{\mathbf{P}}$  is reducible and therefore unable to conform to the strongly monotone criteria in Lemma 3.2. However, we recover the irreducibility of  $\mathbf{P}$  and  $\overline{\mathbf{P}}$  by multiplication with a suitable class of matrices.

**Lemma 3.4.** *Let  $\mathbf{P}$  be the mixed interconnection matrix (2.3) and  $\mathbf{Q} = \text{diag}(\mathbf{Q}_1, \dots, \mathbf{Q}_N)$  be such that  $\mathbf{Q}_k \in \mathbb{R}^{r \times r}$  is irreducible for each  $k \in \{1, \dots, N\}$ . Then  $\mathbf{P}\mathbf{Q}$  is irreducible.*

*Proof.* A graph is said to be strongly connected if there exists a path between any two vertices. We aim to show that the graph defined by the weighted adjacency matrix  $\mathbf{P}\mathbf{Q}$  is strongly connected and therefore use the property that a graph is strongly connected if and only if the associated adjacency matrix is irreducible [11].

For an unweighted, nonnegative adjacency matrix  $\mathbf{M}$ , it can be shown that the  $(i, j)$ th element of  $\mathbf{M}^k$  represents the number of ways to travel from vertex  $v_i$  to vertex  $v_j$  along exactly  $k$  edges. Therefore, if  $\mathbf{M}$  defines a connected graph of  $l$  vertices, then  $\mathbf{M}^l$  contains no zero entries for all  $(i, j)$ ; that is, there exists a path between any two vertices in less than or equal to  $l$  steps [11]. The converse statement is also true. In the case of weighted, nonnegative adjacency matrices, the elements  $(i, j)$  of  $\mathbf{M}^k$  no longer represent the number of ways to get from vertex  $i$  to vertex  $j$  along exactly  $k$  edges but nevertheless are nonzero if there exists a path between  $v_i$  to vertex  $v_j$  along  $k$  or less edges.

The set of vertices has cardinality  $|V_{\mathbf{P}\mathbf{Q}}| = rN$  due to the total number of interconnections within the large-scale IO system (2.1). Hence, consider the adjacency matrix  $(\mathbf{P}\mathbf{Q})^{rN}$ . From Theorem A.3, it can be shown that

$$(3.9) \quad \mathbf{P}^{rN} = \left( \sum_{i=1}^r \mathbf{W}_i \otimes \mathbf{D}_i \right)^{rN} = \sum_{i=1}^r \mathbf{W}_i^{rN} \otimes \mathbf{D}_i,$$

and by the above argument,  $\mathbf{W}_i^{rN}$  has no zero elements, as each  $\mathbf{W}_i$  represents a connected graph of  $N$  vertices. Therefore,  $\mathbf{P}^{rN}$  is the interweave of  $r$  completely nonzero matrices, and thus, without loss of generality, for any nonzero elements  $p_{i,j}$  of  $\mathbf{P}^{rN}$ ,  $p_{i \pm r, j}$  and  $p_{i, j \pm r}$  are also nonzero. Specifically, there exist no two nonzero elements in  $\mathbf{P}^{rN}$  that are more than  $r$  elements apart in each row and column, as in Example 2.1, where  $r = 2, N = 2$ . In addition, define  $\mathbf{Q}_k^{rN} := \tilde{\mathbf{Q}}_k$ . By assumption,  $\tilde{\mathbf{Q}}_k$  has no zero entries for all  $i, j \in \{1, \dots, r\}$  by irreducibility, and so  $\mathbf{Q}^{rN} = \text{diag}(\tilde{\mathbf{Q}}_1, \dots, \tilde{\mathbf{Q}}_N)$ . Applying the definition of the matrix product, the elements of  $(\mathbf{P}\mathbf{Q})^{rN}$  are given by

$$(3.10) \quad (\mathbf{P}^{rN} \mathbf{Q}^{rN})_{ij} = \sum_{k=1}^{rN} p_{i,k} \tilde{q}_{k,j} \neq 0$$

for all  $i, j \in \{1, \dots, rN\}$ , as every column of  $\mathbf{Q}^{rN}$  contains  $r$  consecutive nonzero elements. Therefore,  $(\mathbf{P}\mathbf{Q})^{rN}$  is a nonzero matrix, which implies that the graph of  $\mathbf{P}\mathbf{Q}$  is strongly connected; thus,  $\mathbf{P}\mathbf{Q}$  is irreducible. ■

The statement of Lemma 3.4 applies also to the reduced interconnection matrix  $\bar{\mathbf{P}}$ , as it has identical structure to the corresponding large-scale interconnection matrix  $\mathbf{P}$ , and therefore the irreducibility of the product is preserved under the quotient mapping by  $\pi_2$ . Hence, by ensuring the irreducibility of the Jacobian of the reduced IO system (2.1) spatially coupled by  $\bar{\mathbf{P}}$ , by Lemma 3.4 and (A1), the following statement provides polarity-dependent conditions that guarantee the existence of laminar patterns in semiregular bilayer graphs by using the strongly monotone dynamics of solution trajectories.

**Theorem 3.5 (existence of laminar patterns with semiregular graphs).** *Consider the IO system (2.1) with interconnection matrix  $\mathbf{P}$  (2.3). Let  $\pi_2$  be the layerwise simultaneously equitable partition for all bilayer connectivity graphs,  $\mathcal{G}_k$ , defined by  $\mathbf{P}$  such that the associated reduced interconnection matrix  $\bar{\mathbf{P}}$  (3.4) defines the reduced IO system of representative cells from each layer. Assuming that (A1) is satisfied and there exists  $\bar{\Lambda}_2$  such that the HSS instability condition (2.17) holds for all  $n_{1,\mathcal{L}_i}^{[k]} w_1^{[k]} \leq n_{2,\mathcal{L}_i}^{[k]} w_2^{[k]}$  ( $i \in \{1, 2\}, k \in \{1, \dots, r\}$ ), any solutions in the neighborhood of the HSS,  $\mathbf{x}^*$ , converge to laminar patterns in the reduced system.*

*Proof.* Following from Lemma 2.1, we consider the auxiliary dynamic system defined by the transfer kinetics for the reduced IO system

$$(3.11) \quad \begin{bmatrix} \dot{z}_1 \\ \dot{z}_2 \end{bmatrix} = - \begin{bmatrix} z_1 \\ z_2 \end{bmatrix} + \bar{\mathbf{P}} \begin{bmatrix} \mathbf{T}(z_1) \\ \mathbf{T}(z_2) \end{bmatrix} := \mathbf{F}(z),$$

as this represents the behavior of the reduced IO system using only the spatially dependent components. Note that the fixed points of the auxiliary system (3.11) are those of the IO system (2.1). Namely, the auxiliary system (3.11) has HSS  $\mathbf{z}^* = \mathbf{1}_2 \otimes \mathbf{u}_0$  for the cellwise input steady state  $\mathbf{u}_0$  associated with  $\mathbf{x}^*$ . Linearizing the auxiliary system about the HSS yields the following Jacobian:

$$(3.12) \quad \frac{\partial \mathbf{F}}{\partial \mathbf{z}}(\mathbf{z}^*) = -\mathbf{I}_{2r} + \bar{\mathbf{P}}(\mathbf{I}_2 \otimes \mathcal{DT}(\mathbf{z}^*)).$$

First, we show that the sign structures  $\mathcal{S}_1$  and  $\mathcal{S}_2$  of (A1) are equivalent up to linear transformation on the Jacobian (3.12), thereby ensuring the competitive solution dynamics of the auxiliary system (3.11). Following that, we use a competitive-to-cooperative bijective transformation to show that the auxiliary system is strongly monotone. Critically, the boundedness in combination with strongly monotone kinetics of the transfer function ensures the convergence of heterogeneous solutions in the auxiliary system (3.11) and thus the reduced IO system by Lemma 2.1. A sketch of the following proof is given in Figure 5.

Denote the reflection transformation  $\mathbf{M} = \mathbf{I}_2 \otimes \tilde{\mathbf{M}}$ , where

$$(3.13) \quad \tilde{\mathbf{M}} = \text{diag}((-1), (-1)^2, \dots, (-1)^{r-1}, (-1)^r).$$

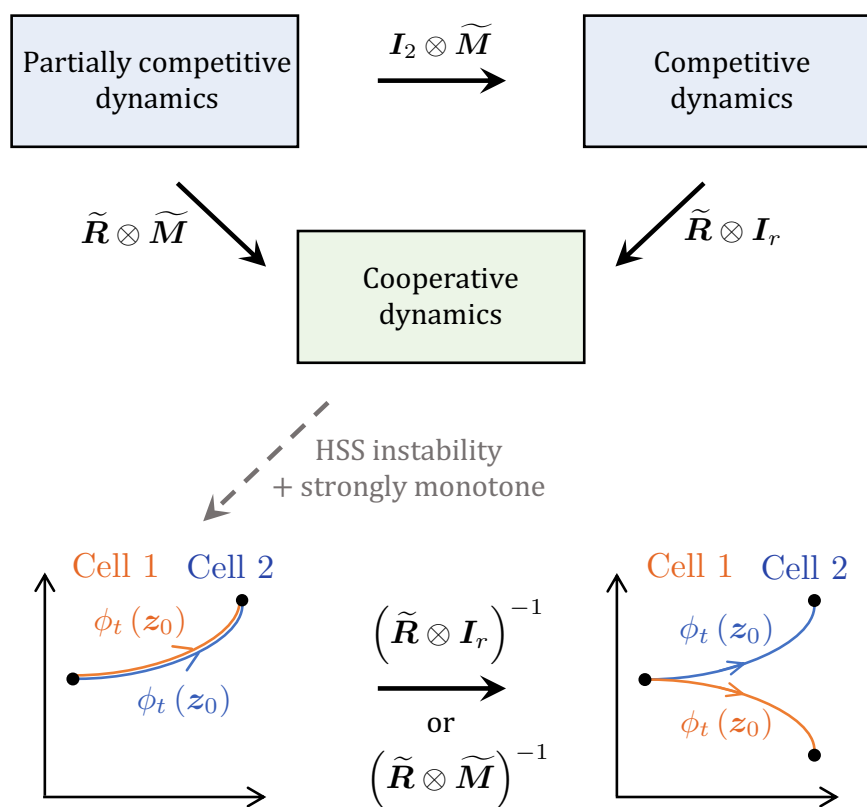


**Figure 5.** A sketch of the proof of Theorem 3.5 for system transformations where  $I_r$  is the identity matrix,  $\tilde{M}$  is the competitive sign structure transformation,  $\tilde{R}$  is the competitive-to-cooperative transformation, and  $\phi_t(z_0)$  is a solution trajectory with initial condition  $z_0$ .

Note that  $\tilde{M}^{-1} = \tilde{M}$  and therefore  $M^{-1} = M$ . We introduce the coordinate transformation  $w = Mz$ , which converts between Jacobians with sign structures  $\mathcal{S}_1$  and  $\mathcal{S}_2$ . Explicitly, consider the auxiliary system (3.11) with  $\text{Sgn}(DT(\cdot)) = \mathcal{S}_2$ . Then the Jacobian (3.12) with respect to  $w$  yields

$$\begin{aligned}
 M \left( \frac{\partial F}{\partial z} (Mw) \right) M &= \left( I_{2r} \otimes \tilde{M} \right) \left( -I_{2r} + \bar{P} (I_2 \otimes DT(Mw)) \right) \left( I_2 \otimes \tilde{M} \right), \\
 &= -I_{2r} + \left( I_2 \otimes \tilde{M} \right) \left( \sum_{i=1}^r \bar{W}_i \otimes D_i \right) \left( I_2 \otimes DT(Mw) \right) \left( I_2 \otimes \tilde{M} \right), \\
 &= -I_{2r} + \left( \sum_{i=1}^r \bar{W}_i \otimes D_i \right) \left( I_2 \otimes \tilde{M} \right) \left( I_2 \otimes DT(Mw) \right) \left( I_2 \otimes \tilde{M} \right), \\
 (3.14) \quad &= -I_{2r} + \left( \sum_{i=1}^r \bar{W}_i \otimes D_i \right) \left( I_2 \otimes \tilde{M} DT(Mw) \tilde{M} \right),
 \end{aligned}$$

where the third and fourth equalities follow from the commutativity of diagonal matrices and the mixed multiplication property of the Kronecker product. The transformed Jacobian (3.14) is a nonpositive matrix as

$$(3.15) \quad \left( \widetilde{\mathbf{M}} \mathcal{DT}(\mathbf{M}\mathbf{w}) \widetilde{\mathbf{M}} \right)_{ij} = (-1)^{i+j} (\mathcal{DT}(\mathbf{M}\mathbf{w}))_{ij}$$

by direct computation. For  $i + j$  odd,  $(\mathcal{DT}(\mathbf{M}\mathbf{w}))_{ij}$  switches sign; i.e.,  $\widetilde{\mathbf{M}} \mathcal{DT}(\mathbf{M}\mathbf{w}) \widetilde{\mathbf{M}}$  has sign structure  $\mathcal{S}_2$ . Therefore, we continue by considering the transfer function with  $\text{Sgn}(\mathcal{DT}(\cdot)) = \mathcal{S}_2$ .

The Jacobian (3.12) with  $\text{Sgn}(\mathcal{DT}(\cdot)) = \mathcal{S}_2$  is a nonpositive matrix, as all elements of  $\overline{\mathbf{P}}$  are nonnegative. From Lemma 3.3, the polarity-dependent eigenvalues  $\lambda_{i,2}$  of  $\overline{\mathbf{W}}_i$  have eigenvectors,  $\mathbf{v}_{i,2}$ , with sign structure  $\text{Sgn}(\mathbf{v}_{i,2}) = [-, +]^T$ . Therefore, motivated by polarity-driven patterning and the requirement of the positivity of the dominant instability mode for monotone kinetics [57], we construct a transformation,  $\mathbf{R}$ , to ensure that any polarity-driven instability satisfies the monotonicity criteria, that is, monotone with respect to alternating domains. Then we consider the transformation  $\mathbf{R} = \widetilde{\mathbf{R}} \otimes \mathbf{I}_r$ , where  $\widetilde{\mathbf{R}} = \text{diag}(-1, 1)$ . Note again that  $\mathbf{R}^{-1} = \mathbf{R}$  as  $\widetilde{\mathbf{R}}^{-1} = \widetilde{\mathbf{R}}$ . By similar calculations as above, it can be shown that by the coordinate transformation  $\mathbf{w} = \mathbf{R}\mathbf{z}$ , the Jacobian (3.12) has the form

$$(3.16) \quad \mathbf{R} \left( \frac{\partial \mathbf{F}}{\partial \mathbf{z}}(\mathbf{R}\mathbf{w}) \right) \mathbf{R} = -\mathbf{I}_{2r} + \sum_{i=1}^r \widetilde{\mathbf{R}} \overline{\mathbf{W}}_i \widetilde{\mathbf{R}} \otimes \mathbf{D}_i \mathcal{DT}(\mathbf{R}\mathbf{w}),$$

where the quotient adjacency matrix is transformed to the following form:

$$(3.17) \quad \widetilde{\mathbf{R}} \overline{\mathbf{W}}_i \widetilde{\mathbf{R}} = \begin{bmatrix} a_i & -(1-a_i) \\ -(1-b_i) & b_i \end{bmatrix}.$$

Therefore, let  $\tau(i) = (i-1) \bmod r + 1$ . Then the row-sum of the transformed auxiliary Jacobian (3.16) can be expressed as

$$(3.18) \quad \sum_{j \neq i} \left( \mathbf{R} \left( \frac{\partial \mathbf{F}}{\partial \mathbf{z}}(\mathbf{R}\mathbf{w}) \right) \mathbf{R} \right)_{ij} = \begin{cases} (2a_{\tau(i)} - 1) \sum_{j=1, i \neq j}^r (\mathbf{D}_{\tau(i)} \mathcal{DT}(\mathbf{R}\mathbf{w}))_{ij} & 1 \leq i \leq r, \\ (2b_{\tau(i)} - 1) \sum_{j=1, i \neq j}^r (\mathbf{D}_{\tau(i)} \mathcal{DT}(\mathbf{R}\mathbf{w}))_{ij} & r+1 \leq i \leq 2r. \end{cases}$$

Hence, by the assumption  $n_{1, \mathcal{L}_i}^{[k]} w_1^{[k]} \leq n_{2, \mathcal{L}_i}^{[k]} w_2^{[k]}$  ( $i \in \{1, 2\}, k \in \{1, \dots, r\}$ ), we have that  $2a_k - 1 \leq 0$  and  $2b_k - 1 \leq 0$  by direct substitution into (3.6). Critically, as  $\mathcal{DT}(\mathbf{R}\mathbf{w})$  is a negative matrix, we have that

$$(3.19) \quad \sum_{j \neq i} \left( \mathbf{R} \left( \frac{\partial \mathbf{F}}{\partial \mathbf{z}}(\mathbf{R}\mathbf{w}) \right) \mathbf{R} \right)_{ij} \geq 0$$

for all  $i \in \{1, \dots, 2r\}$ , thus satisfying the type K condition in Lemma 3.1. Furthermore, by Lemma 3.4, the transformed auxiliary Jacobian (3.16) is irreducible, and therefore the auxiliary dynamical system (3.11) is strongly monotone (cooperative) with respect to the laminar pattern transformation  $\mathbf{R}$ .

The cooperative auxiliary dynamical system (3.11) is monotone with respect to the standard domain  $\mathbb{R}_{\geq 0}^{2r}$  and has a positive eigenvector  $\mathbf{v} > 0$  associated with the polarity-driven

instability  $\overline{\Lambda}_2$  of the transformed HSS  $\mathbf{Rz}^*$  by the Perron–Frobenius theorem [14]. Consequently, for small  $\epsilon$ , any solution starting at  $\mathbf{Rz} = \mathbf{Rz}^* + \epsilon \mathbf{v}$  must have a positive derivative and increase in the transformed trajectory domain  $\mathbb{R}_{\geq 0}^{2r}$  [57]. Critically, if the solutions of the cooperative auxiliary dynamical system (3.11) are bounded, then the strongly monotone property ensures the convergence to another steady state,  $\mathbf{Rz}^{**} \neq \mathbf{Rz}^*$ .

The transfer function  $\mathbf{T}(\cdot)$  is bounded, and so there exists  $b > 0$  such that  $\|\overline{\mathbf{P}}[\mathbf{T}(z_1), \mathbf{T}(z_2)]^T\|_2 < b$  for all  $z_i$ . Thus, as the cooperative auxiliary dynamical system (3.11) is monotone with respect to  $\mathbb{R}_{\geq 0}^{2r}$ , we have that the sets centered about the HSS  $\mathcal{V}_{\pm} = \mathbf{Rz}^* \pm (\mathbb{R}_{\geq 0}^{2r} \cap [0, b]^{2r})$  are forward invariant; i.e.,  $\phi_t(\mathbf{Rz}) \in \mathcal{V}_{\pm}$  for all  $t \in [0, \infty)$ . Therefore, all solutions are bounded within a compact domain and thus converge to  $\mathbf{Rz}^{**} \neq \mathbf{Rz}^*$  by the cooperative irreducible convergence theorem (Theorem 4.3.3 of [57]). Subsequently, the corresponding nontransformed system (3.11) must have all vertices with solutions in  $\mathcal{V}_+$  and  $\mathcal{V}_-$ , respectively, ensuring contrasting cellwise solutions. Finally, as any steady-state solution to the auxiliary dynamical system (3.11) is a steady state of the associated reduced IO system (2.1), by Lemma 2.1, the reduced IO system (2.1) converges to laminar patterns. ■

From Theorem 3.5, we can conclude that the existence of a polarity-driven instability of the HSS implies the existence of heterogeneous steady states within the quotient system. This follows, as solution trajectories diverge when transforming between competitive and cooperative systems, as highlighted in Figure 5. Moreover, as the competitive dynamics of the reduced IO system (2.1) are isomorphic to cooperative dynamics, all periodic solutions are unstable [56], implying the convergence to contrasting cell states. The following example demonstrates how Theorem 3.5 can be applied to prove the existence of laminar patterns in large-scale IO systems.

*Example 3.1.* Consider the DIDO system with two spatially dependent components describing lateral inhibition with a diffusive crosstalk, as represented in Figure 6;

$$(3.20) \quad \dot{x}_{i,1} = g_1(u_{i,1}) \cdot g_2(x_{i,2}) \cdot f_1(u_{i,2}) - x_{i,1},$$

$$(3.21) \quad \dot{x}_{i,2} = f_2(x_{i,1}) - x_{i,2},$$

$$(3.22) \quad \dot{x}_{i,3} = g_3(x_{i,1}) - x_{i,3},$$

$$(3.23) \quad y_{i,1} = x_{i,2},$$

$$(3.24) \quad y_{i,2} = x_{i,3}$$

for each cell  $1 \leq i \leq 60$ . The functions  $f_j$  and  $g_j$ ,  $j = 1, 2, 3$ , are positive, bounded, and increasing and decreasing functions, respectively, of the form

$$(3.25) \quad f_j(x) = \frac{x^{k_j}}{\alpha_j + x^{k_j}} \quad \text{and} \quad g_j(x) = \frac{1}{1 + \beta_j x^{h_j}},$$

where  $\alpha_j, \beta_j, k_j, h_j > 0$ . Let  $u_{i,1}$  and  $u_{i,2}$  be defined by short-range diffusion and contact-based bilayer connectivity graphs  $\mathcal{G}_1$  and  $\mathcal{G}_2$ , respectively, as in Figure 6. Explicitly, we have that outputs are converted to inputs via the global interconnection matrix such that  $\mathbf{u} = (\mathbf{W}_1 \otimes \mathbf{D}_1 + \mathbf{W}_2 \otimes \mathbf{D}_2) \mathbf{y}$  for  $\mathbf{W}_1, \mathbf{W}_2 \in \mathcal{W}$ . Here, we focus on the associated reduced IO system (3.20)–(3.24), which is defined by the simultaneously equitable partition  $\pi_2$ . Namely, in the reduced IO system, outputs are converted to inputs by  $\mathbf{u} = (\overline{\mathbf{W}}_1 \otimes \mathbf{D}_1 + \overline{\mathbf{W}}_2 \otimes \mathbf{D}_2) \mathbf{y}$ ,

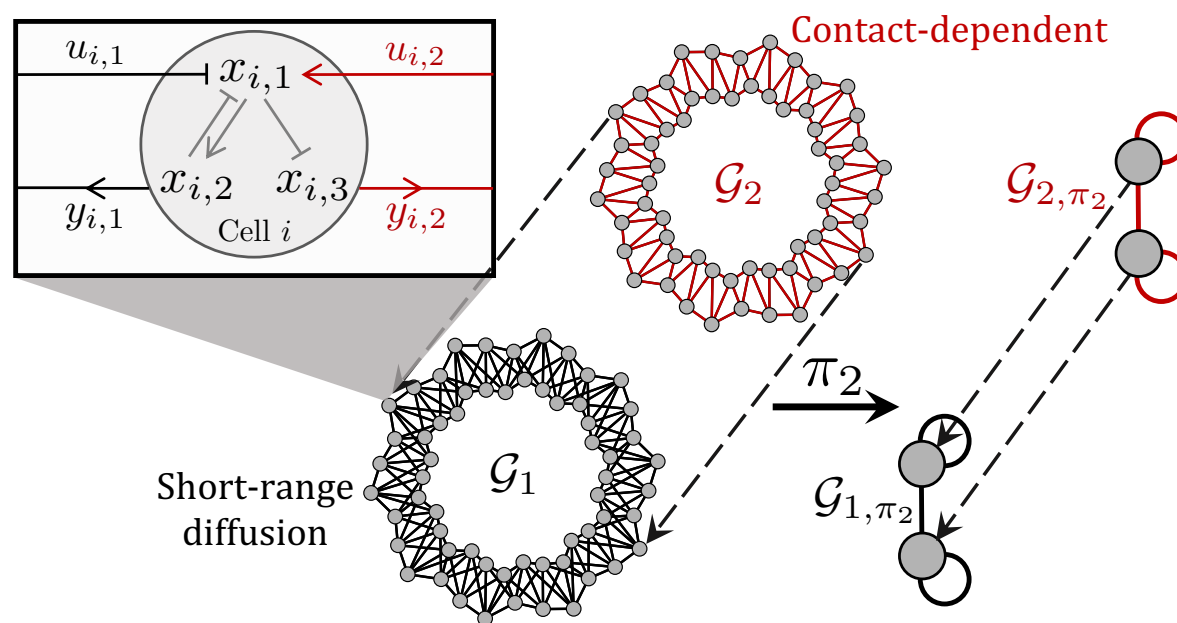


Figure 6. A schematic of the IO system considered in Example 3.1.

where

$$(3.26) \quad \overline{\mathbf{W}}_1 = \begin{bmatrix} 2w_1^{[1]} & 4w_2^{[1]} \\ 2w_1^{[1]}+4w_2^{[1]} & 2w_1^{[1]}+4w_2^{[1]} \\ 4w_2^{[1]} & 2w_1^{[1]} \\ 2w_1^{[1]}+4w_2^{[1]} & 2w_1^{[1]}+4w_2^{[1]} \end{bmatrix} \quad \text{and} \quad \overline{\mathbf{W}}_2 = \begin{bmatrix} 2w_1^{[2]} & 2w_2^{[2]} \\ 2w_1^{[2]}+2w_2^{[2]} & 2w_1^{[1]}+2w_2^{[2]} \\ 2w_2^{[2]} & 2w_1^{[2]} \\ 2w_1^{[2]}+2w_2^{[2]} & 2w_1^{[2]}+2w_2^{[2]} \end{bmatrix}$$

such that  $n_{1,\mathcal{L}_1}^{[1]} = n_{1,\mathcal{L}_2}^{[1]} = n_{1,\mathcal{L}_1}^{[2]} = n_{1,\mathcal{L}_2}^{[2]} = 2$ ,  $n_{2,\mathcal{L}_1}^{[1]} = n_{2,\mathcal{L}_2}^{[1]} = 4$ , and  $n_{2,\mathcal{L}_1}^{[2]} = n_{2,\mathcal{L}_2}^{[2]} = 2$ . We seek to show the existence of polarity-driven laminar patterns using the quotient graphs, and so we first require the HSS of the IO system (3.20)–(3.24) and then derive the derivative of the transfer function  $\mathcal{DT}(\mathbf{u}_i)$ , highlighting that (A1) is satisfied. Applying Theorem 3.5, we generate polarity regimes for the existence of patterning.

The HSS of the IO system (3.20)–(3.24) can be determined by solving

$$(3.27) \quad g_1(f_2(x_1^*)) \cdot g_2(f_2(x_1^*)) \cdot f_1(g_3(x_1^*)) - x_1^* = 0$$

for  $x_1^*$  by setting  $u_{i,1} = x_{i,2}$  and  $u_{i,2} = x_{i,3}$ , conforming to homogeneous input and outputs of the tissue. Furthermore, the HSS defined by solving (3.27) is always stable in the absence of interconnections. This can be shown by considering the linearization of the intracellular kinetics

$$(3.28) \quad \mathbf{A} := \frac{\partial \mathbf{f}}{\partial \mathbf{x}_i} = \begin{bmatrix} -1 & f_1 g_1 g_2' & 0 \\ f_2' & -1 & 0 \\ g_3' & 0 & -1 \end{bmatrix}.$$

As  $\det(\mathbf{A}) = f_1 g_1 f_2' g_2' - 1 < 0$  always holds by the monotonicity of the functions  $f_j$  and  $g_j$ , the HSS defined by solving (3.27) is unique by Lemma 2.2. In addition,  $\mathbf{A}$  has eigenvalues

$$(3.29) \quad \mu_1 = -1, \quad \mu_2 = -1 + \sqrt{f_1 g_1 f_2' g_2'}, \quad \text{and} \quad \mu_3 = -1 - \sqrt{f_1 g_1 f_2' g_2'},$$

and so, as  $\mu_1, \Re(\mu_2), \Re(\mu_3) < 0$ , we have that  $\mathbf{A}$  is stable. Thus, any instability of the HSS will be induced by the interconnection of cells in the tissue.

The derivative of the transfer function can be determined by linearization of the IO kinetics (3.20)–(3.24) as demonstrated in [7] such that  $\mathcal{DT}(\mathbf{u}_i) = -\mathbf{CA}^{-1}\mathbf{B}$ , where  $\mathbf{B}$  and  $\mathbf{C}$  are the linearized inputs and outputs, respectively, as in Lemma 2.3. For the IO system (3.20)–(3.24), the derivative of the transfer function has the form

$$\begin{aligned} \mathcal{DT}(\mathbf{u}_i) &= -\det(\mathbf{A})^{-1} \begin{bmatrix} 0 & 1 & 0 \\ 0 & 0 & 1 \end{bmatrix} \begin{bmatrix} 1 & f_1 g_1 g'_2 & 0 \\ f'_2 & 1 & 0 \\ g'_3 & f_1 g_1 g'_2 g'_3 & 1 - f_1 g_1 g'_2 \end{bmatrix} \begin{bmatrix} f_1 g_2 g'_1 & g_1 g_2 f'_1 \\ 0 & 0 \\ 0 & 0 \end{bmatrix} \\ (3.30) \quad &= -\det(\mathbf{A})^{-1} \begin{bmatrix} f_1 g_2 f'_2 g'_1 & g_1 g_2 f'_1 f'_2 \\ f_1 g_2 g'_1 g'_3 & g_1 g_2 f'_1 g'_3 \end{bmatrix}, \end{aligned}$$

where each of the functions  $f_j$  and  $g_j$  are evaluated using the corresponding arguments for the given input state  $\mathbf{u}_i$ . The multiplication of bounded functions are bounded [35], and subsequently  $\mathcal{DT}(\mathbf{u}_i)$  is elementwise bounded, as  $f_j, g_j, f'_j$ , and  $g'_j$  are bounded. In addition, from the monotonicity of  $f_j$  and  $g_j$ , we have that

$$(3.31) \quad \text{Sgn}(\mathcal{DT}(\mathbf{u}_i)) = \begin{bmatrix} - & + \\ + & - \end{bmatrix} = \mathcal{S}_1,$$

and so the IO system (3.20)–(3.24) satisfies (A1). Therefore, by Theorem 3.5, we have that the IO system (3.20)–(3.24) is spatially coupled using the quotient graphs  $\mathcal{G}_{1,\pi_2}$  and  $\mathcal{G}_{2,\pi_2}$ ; the instability of the HSS in addition to the monotone polarity conditions  $w_1^{[1]} \leq 2w_2^{[1]}$  and  $w_1^{[2]} \leq w_2^{[2]}$  produce contrasting cellwise states.

By Corollary 2.6, we apply the DIDO instability inequality (2.21) to the IO system (3.20)–(3.24). As  $\det(\mathcal{DT}(\mathbf{u}_i)) = 0$ , the DIDO instability inequality (2.21) reduces to  $1 < \text{tr}(\overline{\Lambda}_2 \mathcal{DT}(\mathbf{u}_i))$ ; namely, the HSS is unstable only if

$$(3.32) \quad 1 < -\det(\mathbf{A})^{-1} \left( \left( \frac{w_1^{[1]} - 2w_2^{[1]}}{w_1^{[1]} + 2w_2^{[1]}} \right) f_1 g_2 g'_1 f'_2 + \left( \frac{w_1^{[2]} - w_2^{[2]}}{w_1^{[2]} + w_2^{[2]}} \right) g_1 g_2 f'_1 g'_3 \right)$$

for the reduced IO system (3.20)–(3.24). The monotone polarity conditions  $w_1^{[1]} \leq 2w_2^{[1]}$  and  $w_1^{[2]} \leq w_2^{[2]}$  of Theorem 2.5 confirm that each of the reduced connectivity matrices must have negative eigenvalues to produce the instability of the HSS, as  $f_1 g_2 g'_1 f'_2 < 0$  and  $g_1 g_2 f'_1 g'_3 < 0$ . Critically, the HSS instability inequality (3.32) highlights that as the layerwise activator/receptor polarity increases, i.e.,  $w_1^{[i]} \ll w_2^{[i]}$ , the potential to induce laminar patterns also increases in the quotient system. Then by the spectral retention property of the equitable partition  $\pi_2$ , we have that laminar patterns must exist in the pattern space of the associated large-scale system.

To illustrate the application Theorem 3.5 to the IO system (3.20)–(3.24), numerical verification of the polarity parameter regime for laminar pattern existence determined by inequality (3.32) is given in Figure 7.

As demonstrated in Example 3.1, the method of pattern templating for contrasting solutions between cells in opposing layers can be used to show the existence of layerwise differing

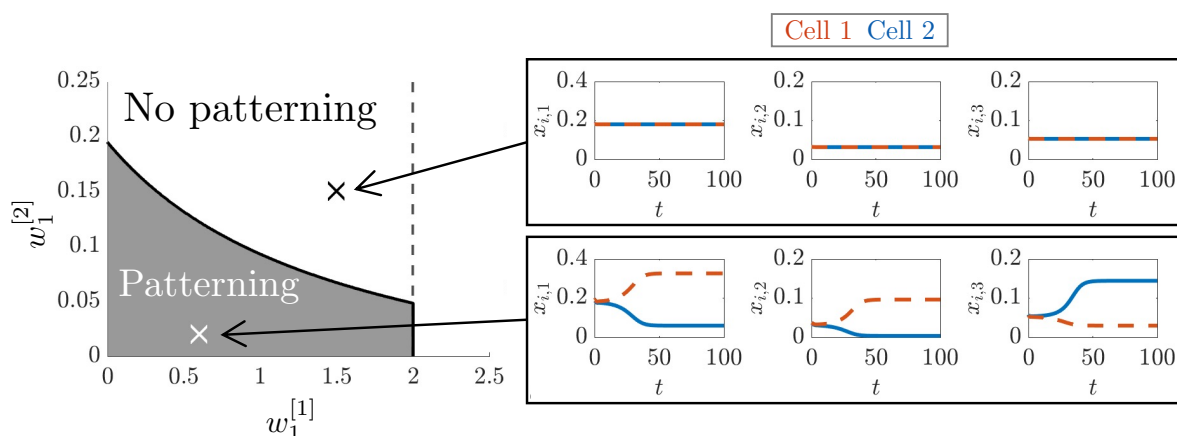
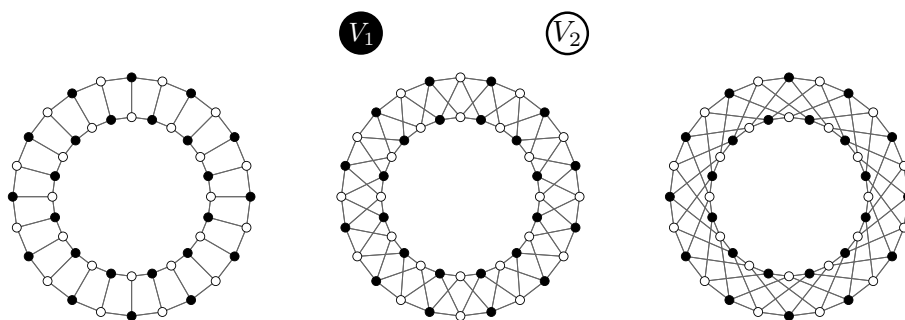


**Figure 7.** Polarity parameter regimes for the existence of laminar patterns in the IO system (3.20)–(3.24). For fixed  $w_2^{[1]} = w_2^{[2]} = 1$ , inequality (3.32) in addition to the monotone polarity conditions  $w_1^{[1]} \leq w_2^{[1]}$  and  $w_1^{[2]} \leq 2w_2^{[2]}$  define regions in  $(w_1^{[1]}, w_1^{[2]})$ -space for the existence of laminar patterns. The dashed line in the  $(w_1^{[1]}, w_1^{[2]})$ -space corresponds to the monotone condition  $w_1^{[1]} \leq 2w_2^{[1]}$ . Example simulations are given for polarity parameter values inside the pattern region (0.6, 0.02) and outside the pattern region (1.5, 0.15). Initial conditions were given as small random perturbations about the HSS,  $\mathbf{x}^* = [0.18, 0.03, 0.05]^T$ . IO system (3.20)–(3.24) parameter values and details on simulations are given in Appendix B.

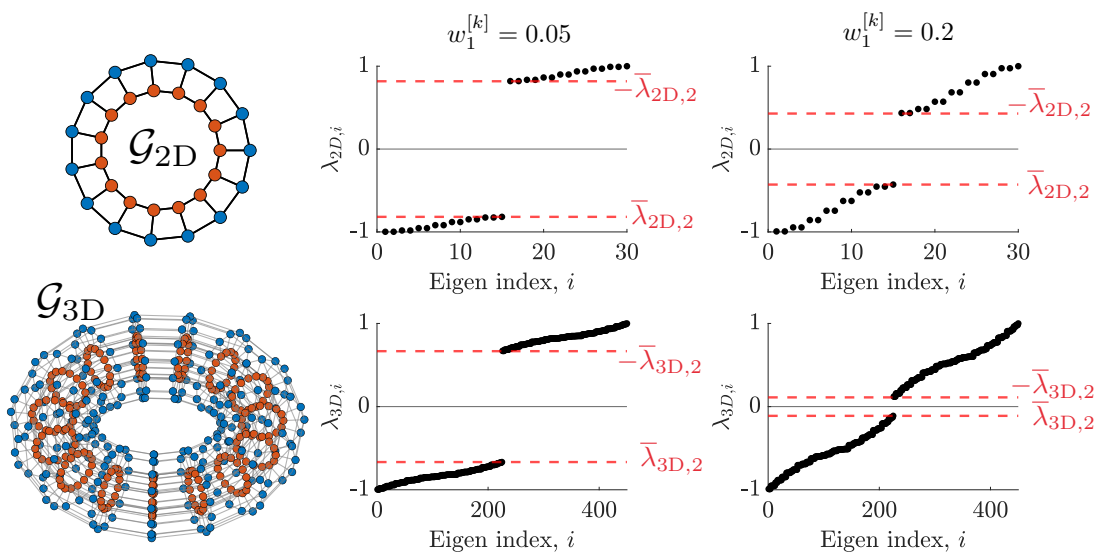
steady states via polarity-driven instabilities. However, the associated large-scale systems may have many locally stable steady states that produce the pattern space of the IO system which could have been lost during the dimension-reducing transformation by the partition,  $\pi_2$  [52]. Therefore, in the following section, we investigate the spectral properties of the bilayer connectivity graphs to ensure that the laminar patterns produced by Theorem 3.5 are indeed globally dominant.

**3.3. Spectral links between quotient and large-scale bilayer connectivity graphs.** For linearized dynamical systems near steady state, the local solution trajectories are a linear combination of the associated eigenvectors scaled by the corresponding exponent of the eigenvalues [48]. Thus, in the instance of steady-state instability, all trajectories close to the steady state will locally tend in the direction of the eigenvector associated with the largest real-part eigenvalue. Critically, to ensure the monotone convergence of laminar patterns in the reduced IO systems in Theorem 3.5, we transformed the polarity-dependent eigenvector to be directed in the positive orthant, conforming to the behavior of cooperative dynamics. Thus, motivated by this positive direction transformation, we seek to understand when the eigenvalue associated with laminar pattern formation dominates the large-scale spectra. This ensures that the perturbed trajectories from the HSS are preferably pointed in the direction to achieve layerwise contrasting states in the large-scale IO systems.

Previous studies on pattern formation using IO systems have imposed the sufficient condition that the large-scale and quotient multilayer connectivity graphs  $\mathcal{G}_k$  are bipartite, as this generates monotone dynamics with respect to the bipartition vector [7, 25, 26, 52]. Namely, a graph  $\mathcal{G}_k$  is said to be bipartite if the vertices  $v \in V$  can be partitioned into two independent sets  $V_1$  and  $V_2$  such that no two vertices in the same set are adjacent [20]. Example bipartite bilayer graphs are given in Figure 8(A). However, it can be demonstrated that for



(a) Bipartite bilayer graphs.



(b) Example spectra of bipartite bilayers.

**Figure 8.** Structure and spectra of bipartite bilayer connectivity graphs. (A) Example regular bipartite graphs where vertices are colored with respect to the bipartition sets  $V_1$  and  $V_2$  in black and white, respectively. (B) Spectra of two bipartite graphs  $\mathcal{G}_{2D}$  and  $\mathcal{G}_{3D}$  are shown for  $w_1^{[k]} = 0.05$  and  $w_1^{[k]} = 0.2$  for fixed  $w_2^{[k]} = 1$  ( $k \in \{2D, 3D\}$ ), where the eigen index refers to the position of the eigenvalue when listed in ascending order. The dashed red lines correspond to the polarity-dependent eigenvalue  $\bar{\lambda}_{k,2}$ , highlighting its position with respect to the ascending spectrum of the associated large-scale graph. The vertices of the graphs are colored layerwise to emphasize their bilayer structure.

bipartite bilayer graphs, the polarity-dependent eigenvalue,  $\bar{\lambda}_{k,2}$ , associated with laminar pattern formation cannot be dominant.

**Lemma 3.6.** Let  $\mathcal{G}_k$  be a bipartite bilayer graph with weighted adjacency matrix  $\mathbf{W}_k \in \mathcal{W}$ . Then for any  $w_1^{[k]}, w_2^{[k]} > 0$ , the polarity-dependent eigenvalue  $\bar{\lambda}_{k,2}$  associated with the reduced adjacency matrix  $\overline{\mathbf{W}}_k$  satisfies

$$(3.33) \quad \bar{\lambda}_{k,2} \neq \min(\text{Spec}(\mathbf{W}_k)).$$

*Proof.* Consider  $\lambda_{k,j} \in \text{Spec}(\mathbf{W}_k)$ . Then by the spectral symmetry of bipartite graphs about the origin, we have that  $-\lambda_{k,j} \in \text{Spec}(\mathbf{W}_k)$  [20]. As  $\mathbf{W}_k \in \mathcal{W}$ ,  $\lambda_{k,1} = \max(\text{Spec}(\mathbf{W}_k)) = 1$  by the connected and row-stochastic properties of  $\mathbf{W}_k$  [34]. Consequently,  $-\lambda_{k,1} = \min(\text{Spec}(\mathbf{W}_k)) = -1$ . However, the minimal eigenvalue of the reduced adjacency matrix  $\overline{\mathbf{W}}_k$  defined by the laminar pattern partition,  $\pi_2$ , must be of the form  $\bar{\lambda}_{k,2} = a_k + b_k - 1$  for  $a_k, b_k \in (0, 1)$  by Lemma 3.3. Critically, this implies that  $\bar{\lambda}_{k,2} \in (-1, 1)$  and therefore  $\bar{\lambda}_{k,2} \neq \min(\text{Spec}(\mathbf{W}_k))$  for any layer-wise polarity values  $w_1^{[k]}, w_2^{[k]} > 0$ . ■

A direct consequence of Lemma 3.6 is that if the large-scale IO system (2.1) is spatially coupled by a bipartite bilayer graph  $\mathcal{G}_k$ , then any trajectory initiated from a small perturbation of an unstable HSS will not be dominantly traveling in the direction of the eigenvector associated with laminar patterning. Critically, there will always exist a greater instability mode of the IO system (2.1). Figure 8(B) demonstrates the consequences of Lemma 3.6, and for the given bipartite graphs, the laminar patterning polarity-dependent eigenvalue  $\bar{\lambda}_{k,2}$  defines a spectral gap about the origin which is proved in Appendix C.

Following Lemma 3.6, we focus our attention on the spectral investigation of nonbipartite semiregular bilayer graphs. As we are interested in the polarity-driven pattern events using a predefined pattern template,  $\pi_2$ , we seek layerwise polarity conditions in which  $\bar{\lambda}_{k,2}$  becomes minimal. Subsequently, we considered a variety of nonbipartite graphs, each with different edge connectivity structure, and varied the same-layer weighting parameter  $w_1^{[k]}$  for fixed  $w_2^{[k]} = 1$ , measuring the position of  $\bar{\lambda}_{k,2}$  in terms of the ascending spectrum of the associated large-scale graph. A summary of the nonbipartite connectivity structures that were considered is in given in Table 2 in Appendix B.

For each of the nonbipartite bilayer graphs that were considered, we observed that decreasing the same-layer weighting parameter,  $w_1^{[k]}$ , shifted the eigenvalue  $\bar{\lambda}_{k,2}$  associated with laminar pattern formation toward the minimum of the spectrum (Figure 9). Furthermore, we demonstrate that  $\bar{\lambda}_{k,2} = \min(\text{Spec}(\mathbf{W}_k))$  for values of  $w_1^{[k]} < w_2^{[k]}$ , noting that this was achieved for higher values of  $w_1^{[k]}$  in the graphs with more cross-layer connections than same-layer connections,  $n_{1,\mathcal{L}_i} < n_{2,\mathcal{L}_i}$ . Critically, Figure 9 highlights that there exists large-scale non-bipartite connectivity graphs that have the capacity to be fully characterized by the extrema of the spectrum of the laminar quotient graph by control of the amount of polarity in the system. That is, with high layerwise polarity,  $w_1^{[k]} \ll w_2^{[k]}$ , we have  $\min(\text{Spec}(\overline{\mathbf{W}}_k)) = \min(\text{Spec}(\mathbf{W}_k))$  and  $\max(\text{Spec}(\overline{\mathbf{W}}_k)) = \max(\text{Spec}(\mathbf{W}_k))$ .

By Theorem 3.5, we demonstrated that the existence of laminar patterns with competitive kinetics is dependent on the existence of connectivity polarity within the quotient connectivity graphs to induce both HSS instability and monotonicity of solutions. Therefore, in the following section, we explore whether solution behaviors observed in the reduced systems are preserved in the associated large-scale systems when the quotient graphs preserve the extrema of the spectra of the large-scale graphs. Namely, we show that the analysis conducted on the reduced IO systems yields global pattern convergence in high-polarity regimes. Specifically, we say that the large-scale IO system (2.1) globally converges to laminar patterns if  $\mathbf{x}$  conforms to Definition 2.1 for all sufficiently small perturbations about the HSS,  $\mathbf{x}^*$ .

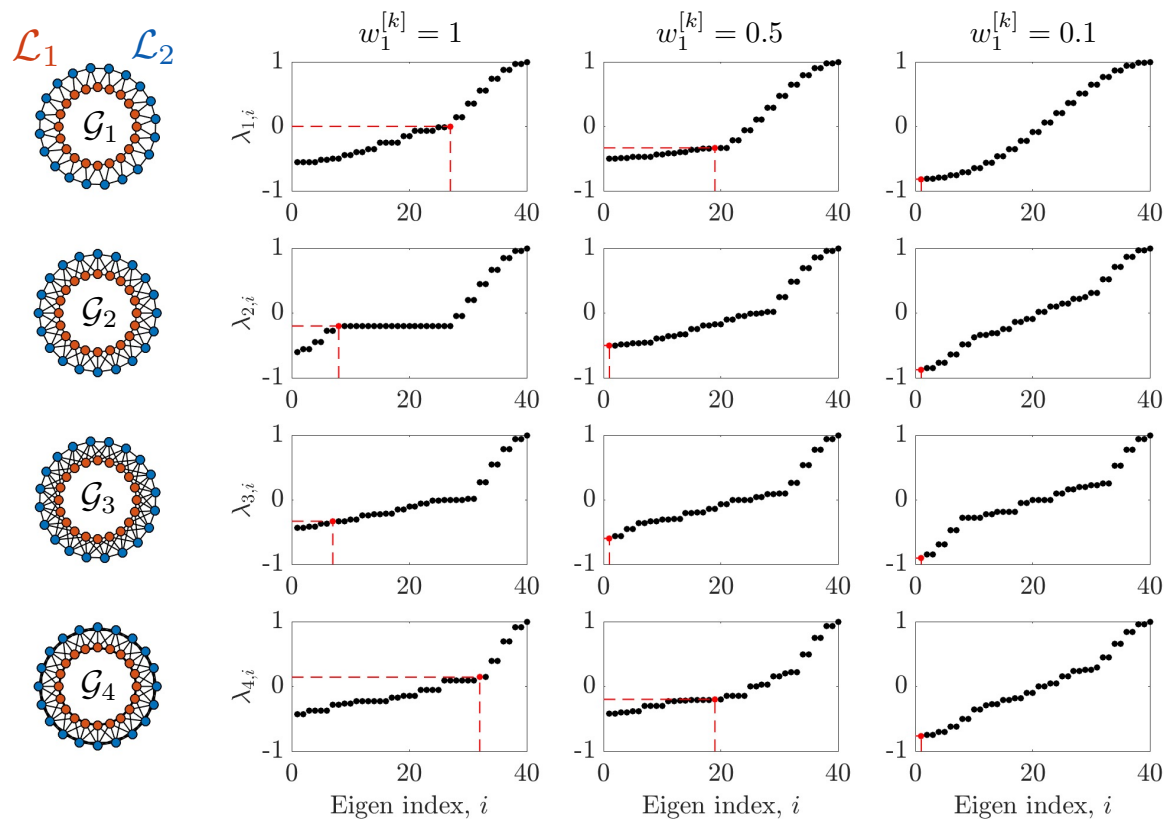


**Figure 9.** Eigenvalues associated with laminar pattern trajectories tend to the minimum of the large-scale spectra as polarity increases in nonbipartite bilayer graphs. The nonbipartite graphs  $\mathcal{G}_k$  ( $k = 1, 2, 3, 4$ ) are shown on the left with vertices colored layerwise. The spectrum of each graph is then shown in ascending order for same-layer polarity values  $w_1^{[k]} = 1$ ,  $w_1^{[k]} = 0.5$ , and  $w_1^{[k]} = 0.1$ , where the eigen index corresponds to the increasing ordering of the eigenvalues. In each of the plots,  $\lambda_{k,2}$  is highlighted in red with dashed lines included to emphasize the value position in the ascending ordering of eigenvalues. Details on the connectivity structures each of the graphs are provided in Appendix B.

**3.4. Polarity-induced laminar pattern formation derived by quotient systems for large-scale bilayer geometries.** In this section, we investigate the conditions in which the patterns predicted using the dimension reduction technique of quotient templating are the globally dominant patterns produced in the large-scale IO systems. We have demonstrated in section 3.3 that the spectra of nonbipartite semiregular bilayer connectivity graphs have the capacity to be bounded by the extrema of the spectra of the associated quotient graphs defined by  $\pi_2$ . This implies that the polarity-driven HSS instability imposed by the pattern existence condition of Theorem 3.5 in the quotient systems must also exist in the large-scale systems and can become dominant in high-polarity regimes. Therefore, we now focus our attention on whether the large-scale IO system is monotone with respect to the eigenvector locally directing solutions to laminar patterns, thus preserving trajectory direction.

**Lemma 3.7.** Consider the large-scale IO system (2.1) spatially coupled by the global adjacency matrix  $\mathbf{P}$  (2.3), where  $\mathbf{W}_k \in \mathcal{W}$  for  $k \in \{1, \dots, r\}$ . Assuming that (A1) is satisfied and

the laminar pattern partition,  $\pi_2$ , is simultaneously equitable, if all connectivity graphs  $\mathcal{G}_k$  are highly polarized,  $w_1^{[k]} \ll w_2^{[k]}$ , the large-scale IO system (2.1) generates monotone solutions in the direction of laminar patterns.

*Proof.* Similar to Theorem 3.5, we consider the large-scale auxiliary system

$$(3.34) \quad \begin{bmatrix} \dot{z}_1 \\ \vdots \\ \dot{z}_N \end{bmatrix} = - \begin{bmatrix} z_1 \\ \vdots \\ z_N \end{bmatrix} + \mathbf{P} \begin{bmatrix} \mathbf{T}(z_1) \\ \vdots \\ \mathbf{T}(z_N) \end{bmatrix} := \mathbf{F}(\mathbf{z}),$$

which has the identical behavior to the large-scale IO system (2.1) by Lemma 2.1, yet the auxiliary system (3.34) only explicitly considers the spatially dependent components of the model. First, we will construct the sign structure of the eigenvector associated with laminar patterns in the large-scale graphs. Then, by transforming the auxiliary system (3.34) to ensure the positivity of the laminar pattern eigenvector, we demonstrate that the large-scale IO system (2.1) has the capacity to become type K for high-polarity bilayers.

Linearizing the auxiliary system (3.34) about a generic point  $\mathbf{z} \in \mathbb{R}_{\geq}^{rN}$  yields

$$(3.35) \quad \frac{\partial \mathbf{F}}{\partial \mathbf{z}} = -\mathbf{I}_{rN} + \mathbf{P} \begin{bmatrix} \mathcal{DT}(z_1) & & \\ & \ddots & \\ & & \mathcal{DT}(z_N) \end{bmatrix},$$

where  $\mathbf{T}(\cdot)$  satisfies (A1) and thus  $\text{sgn}(\mathcal{DT}) = \mathcal{S}_1$  or  $\text{sgn}(\mathcal{DT}) = \mathcal{S}_2$ . As in the proof of Theorem 3.5, the transformation  $\mathbf{M} = \mathbf{I}_N \otimes \widetilde{\mathbf{M}}$ , where  $\widetilde{\mathbf{M}}$  as given in (3.13), demonstrates the equivalence of the sign structures. That is, if  $\text{sgn}(\mathcal{DT}) = \mathcal{S}_1$ , then  $\text{sgn}(\widetilde{\mathbf{M}}^T \mathcal{DT} \widetilde{\mathbf{M}}) = \mathcal{S}_2$ . Therefore, we continue assuming  $\text{sgn}(\mathcal{DT}) = \mathcal{S}_2$ , critically that  $\text{diag}(\mathcal{DT}(z_1), \dots, \mathcal{DT}(z_N))$  is a nonpositive matrix.

The reduced graphs associated with the laminar pattern template  $\mathcal{G}_{k,\pi_2}$  have eigenvalues  $\bar{\lambda}_{k,1} = 1$  and  $\bar{\lambda}_{k,2} = a_k + b_k - 1$  with eigenvectors  $\bar{\mathbf{v}}_{k,1} = [1, 1]^T$  and  $\bar{\mathbf{v}}_{k,2} = [1, (b_k - 1) / (1 - a_k)]^T$ , noting that  $a_k, b_k \in (0, 1)$  by definition of the reduced adjacency matrix  $\bar{\mathbf{W}}_k$  (3.5). Subsequently, the polarity-dependent eigenvector has sign structure  $\text{sgn}(\bar{\mathbf{v}}_{k,2}) = [+,-]^T$ . Furthermore, as  $\pi_2$  is equitable for all graphs  $\mathcal{G}_k$ , there exists a matrix  $\mathbf{L} \in \{0, 1\}^{N \times 2}$  that maps the large-scale graph into the quotient graph such that

$$(3.36) \quad \mathbf{L} \bar{\mathbf{W}}_k = \mathbf{W}_k \mathbf{L},$$

where  $\mathbf{L}$  allocates the vertices of the large-scale system into the reduced groups associated with the laminar pattern template [20]. Due to the layerwise vertex indexing as constructed in section 2.1, we have that

$$(3.37) \quad \mathbf{L} = \begin{bmatrix} \mathbf{1}_{|\mathcal{L}_1| \times 1} & \mathbf{0}_{|\mathcal{L}_1| \times 1} \\ \mathbf{0}_{|\mathcal{L}_2| \times 1} & \mathbf{1}_{|\mathcal{L}_2| \times 1} \end{bmatrix}.$$

From the quotient to large-scale algebraic relation (3.36), we have that  $\mathbf{L} \bar{\mathbf{v}}_{k,2}$  is an eigenvector of  $\mathbf{W}_k$  with eigenvalue  $\bar{\lambda}_{k,2}$ . Specifically, this implies that the eigenvector associated with laminar patterning in the large-scale graphs has the sign structure  $\text{sgn}(\mathbf{L} \bar{\mathbf{v}}_{k,2}) =$

$[+, \dots, +, -, \dots, -]^T_2$  which has  $|\mathcal{L}_1|$  and  $|\mathcal{L}_2|$  positive and negative entries, respectively. Hence, the matrix  $\mathbf{R} = \text{diag}(1, \dots, 1, -1, \dots, -1)$  orients the laminar patterning eigenvector  $\mathbf{L}\bar{\mathbf{v}}_{k,2}$  in the positive orthant, i.e.,  $\tilde{\mathbf{R}}\mathbf{L}\bar{\mathbf{v}}_{k,2} > 0$ .

We next introduce the transformation  $\mathbf{w} = \mathbf{R}\mathbf{z}$ , where  $\mathbf{R} = \tilde{\mathbf{R}} \otimes \mathbf{I}_r$ , noting that  $\mathbf{R}^{-1} = \mathbf{R}$ . Following this change of variables, let  $\mathbf{X}_1 = \text{diag}(\mathcal{DT}(z_1), \dots, \mathcal{DT}(z_{|\mathcal{L}_1|}))$  and  $\mathbf{X}_2 = \text{diag}(\mathcal{DT}(z_{|\mathcal{L}_1|+1}), \dots, \mathcal{DT}(z_N))$  be nonpositive matrices. Then in combination with the layerwise block formulation of the bilayer adjacency matrices,  $\mathbf{W}_k$ , the linearized auxiliary system (3.35) has the form

$$\begin{aligned}
 \mathbf{R} \frac{\partial \mathbf{F}}{\partial \mathbf{z}} \mathbf{R} &= -\mathbf{I}_{rN} + \mathbf{R}\mathbf{P} \begin{bmatrix} \mathbf{X}_1 & \mathbf{0} \\ \mathbf{0} & \mathbf{X}_2 \end{bmatrix} \mathbf{R}, \\
 &= -\mathbf{I}_{rN} + \left( \sum_{i=1}^r \tilde{\mathbf{R}}\mathbf{W}_i \otimes \mathbf{D}_i \right) \cdot \begin{bmatrix} \mathbf{X}_1 & \mathbf{0} \\ \mathbf{0} & -\mathbf{X}_2 \end{bmatrix}, \\
 &= -\mathbf{I}_{rN} + \left( \sum_{i=1}^r \begin{bmatrix} \widehat{\mathbf{W}}_{1,\mathcal{L}_1}^{[i]} \otimes \mathbf{D}_i & \widehat{\mathbf{W}}_{2,\mathcal{L}_1}^{[i]} \otimes \mathbf{D}_i \\ -\left(\widehat{\mathbf{W}}_{2,\mathcal{L}_1}^{[i]}\right)^T \otimes \mathbf{D}_i & -\widehat{\mathbf{W}}_{1,\mathcal{L}_2}^{[i]} \otimes \mathbf{D}_i \end{bmatrix} \right) \cdot \begin{bmatrix} \mathbf{X}_1 & \mathbf{0} \\ \mathbf{0} & -\mathbf{X}_2 \end{bmatrix}, \\
 (3.38) \quad &= -\mathbf{I}_{rN} + \sum_{i=1}^r \begin{bmatrix} \left(\widehat{\mathbf{W}}_{1,\mathcal{L}_1}^{[i]} \otimes \mathbf{D}_i\right) \mathbf{X}_1 & -\left(\widehat{\mathbf{W}}_{2,\mathcal{L}_1}^{[i]} \otimes \mathbf{D}_i\right) \mathbf{X}_2 \\ -\left(\left(\widehat{\mathbf{W}}_{2,\mathcal{L}_1}^{[i]}\right)^T \otimes \mathbf{D}_i\right) \mathbf{X}_1 & \left(\widehat{\mathbf{W}}_{1,\mathcal{L}_2}^{[i]} \otimes \mathbf{D}_i\right) \mathbf{X}_2 \end{bmatrix}
 \end{aligned}$$

by the mixed-product and block-product properties of the Kronecker product [24]. The transformed auxiliary system (3.38) is monotone if the off-diagonal row-sum is nonnegative by Lemma 3.1. Namely, if  $\tau(i) = (i - 1) \bmod r + 1$ , then

$$(3.39) \quad \sum_{j \neq i} \left( \mathbf{R} \frac{\partial \mathbf{F}}{\partial \mathbf{z}} \mathbf{R} \right)_{ij} = \begin{cases} \hat{w}_1^{[\tau(i)]} \sum_{j=1, j \neq i}^{r|\mathcal{L}_1|} (\mathbf{X}_1)_{\tau(i)j} - \hat{w}_2^{[\tau(i)]} \sum_{j=1, j \neq i}^{r|\mathcal{L}_2|} (\mathbf{X}_2)_{\tau(i)j} & 1 \leq i \leq r|\mathcal{L}_1|, \\ -\hat{w}_2^{[\tau(i)]} \sum_{j=1, j \neq i}^{r|\mathcal{L}_1|} (\mathbf{X}_1)_{\tau(i)j} + \hat{w}_1^{[\tau(i)]} \sum_{j=1, j \neq i}^{r|\mathcal{L}_2|} (\mathbf{X}_2)_{\tau(i)j} & r|\mathcal{L}_1| + 1 \leq i \leq rN. \end{cases}$$

In particular, as  $\text{sgn}(\mathcal{DT}) = \mathcal{S}_2$ , all positive and negative components of the row-sum are scaled by  $w_2^{[k]}$  and  $w_1^{[k]}$ , respectively. Then for sufficiently small values of  $w_1^{[k]}$  combined with relatively large values  $w_2^{[k]}$ , confirmed by  $w_1^{[k]} \ll w_2^{[k]}$ , we have that

$$(3.40) \quad \sum_{j \neq i} \left( \mathbf{R} \frac{\partial \mathbf{F}}{\partial \mathbf{z}} \mathbf{R} \right)_{ij} \geq 0$$

for all  $1 \leq i \leq rN$ . Therefore, the auxiliary system (3.34) is type K by Lemma 3.1 and so is monotone in the direction for solutions associated with laminar patterning in high-polarity regimes. ■

Applying the cooperative transformation in high-polarity regimes to an IO system (2.1) where the extrema of the spectra are preserved in the quotient mapping guarantees the global convergence of laminar patterns in the large-scale systems. Critically, this extends the existence statement of Theorem 3.5 to sufficient conditions for large-scale laminar patterning.

**Theorem 3.8** (global convergence of laminar patterns in highly polarized regimes). *Consider the large-scale IO system (2.1) spatially coupled by the global adjacency matrix  $\mathbf{P}$  (2.3), where  $\mathbf{W}_k \in \mathcal{W}$  for  $k \in \{1, \dots, r\}$ . Assuming that (A1) is satisfied, the laminar pattern partition  $\pi_2$  is simultaneously equitable, and each connectivity graph,  $\mathcal{G}_k$ , is highly polarized,  $w_1^{[k]} \ll w_2^{[k]}$ . If  $\bar{\lambda}_{k,2} = \min(\text{Spec}(\mathbf{W}_k))$  such that the laminar pattern existence criterion, Theorem 3.5, is satisfied, then laminar patterns are globally convergent in the large-scale IO system (2.1).*

*Proof.* Following Theorem 3.5, by analyzing the quotient graphs, there exists  $\bar{\Lambda}_2$  such that the HSS instability condition (2.17) is satisfied. In addition, Lemma 3.7 guarantees that the IO system (2.1) generates monotone solutions in the direction of laminar patterns such that the eigenvector associated with  $\bar{\lambda}_{k,2}$  is directed in the positive orthant,  $\bar{\mathbf{R}}\mathbf{L}\bar{\mathbf{v}}_{k,2} > 0$ . Furthermore, Lemma 3.4 ensures that the linearized IO system is irreducible, and thus the IO system (2.1) is strongly monotone by Lemma 3.2.

By the identical arguments of Theorem 3.5, the corresponding large-scale auxiliary system (3.35) has bounded solutions, inducing the convergence of solutions to steady state  $\mathbf{R}\mathbf{z}^{**} \neq \mathbf{R}\mathbf{z}^*$  by the cooperative irreducible convergence theorem (Theorem 4.3.3 of [57]). Critically, mapping back to the original coordinating system guarantees that vertices in different layers have contrasting solutions. ■

The sufficient conditions for large-scale laminar patterning outlined in Theorem 3.8 ensure that the behavior observed in the quotient systems is preserved in the corresponding large-scale systems. Subsequently, this enables an analytic approach to pattern prediction, as we can fully determine the spectra of the quotient graphs  $\mathcal{G}_2$  independently and without imposing commutativity conditions on the reduced adjacency matrices. The following example demonstrates the accessibility of the analysis for large-scale IO systems' spatially coupled multilayer connectivity graphs.

**Example 3.2.** We revisit Example 3.1 to seek a polarity regime that guarantees the global convergence of laminar patterns using analysis conducted in the quotient systems when templating the large-scale system using the equitable partition,  $\pi_2$ . Namely, in conjunction with the results of applying Theorem 3.5 to the DIDO system (3.20)–(3.24) as in Example 3.1, we also invoke Theorem 3.8 to isolate regions of polarity parameter values for  $w_1^{[1]}$  and  $w_1^{[2]}$  in which the extrema of the quotient graph spectra are the extrema of the large-scale graphs.

As each of the connectivity large-scale and quotient graphs are row-stochastic, we always have

$$(3.41) \quad \max(\text{Spec}(\bar{\mathbf{W}}_k)) = \max(\text{Spec}(\mathbf{W}_k)) = 1;$$

therefore, the quotient graphs retain the maximum eigenvalues, and so now we focus on the preservation of the minimal eigenvalues.

In Figure 9, we have demonstrated that for  $w_1^{[k]} < 0.5$  and  $w_2^{[k]} = 1$ , the quotient connectivity graphs for short-range diffusion and contact-dependent signaling mechanisms,  $\mathcal{G}_{1,\pi_2}$  and  $\mathcal{G}_{2,\pi_2}$  (which are denoted  $\mathcal{G}_1$  and  $\mathcal{G}_3$  in Figure 9, respectively), have the capacity to bound the spectra of the large-scale graphs  $\mathcal{G}_1$  and  $\mathcal{G}_2$  from below. Critically, this implies that for any  $w_1^{[k]} < 0.5$  with fixed  $w_2^{[k]} = 1$ , which induced HSS instability, solutions will be locally directed toward laminar patterning, and so, following from Theorem 3.8, for sufficiently small  $w_1^{[k]} < 0.5$ , the large-scale DIDO system (3.20)–(3.24) will converge to laminar patterns.

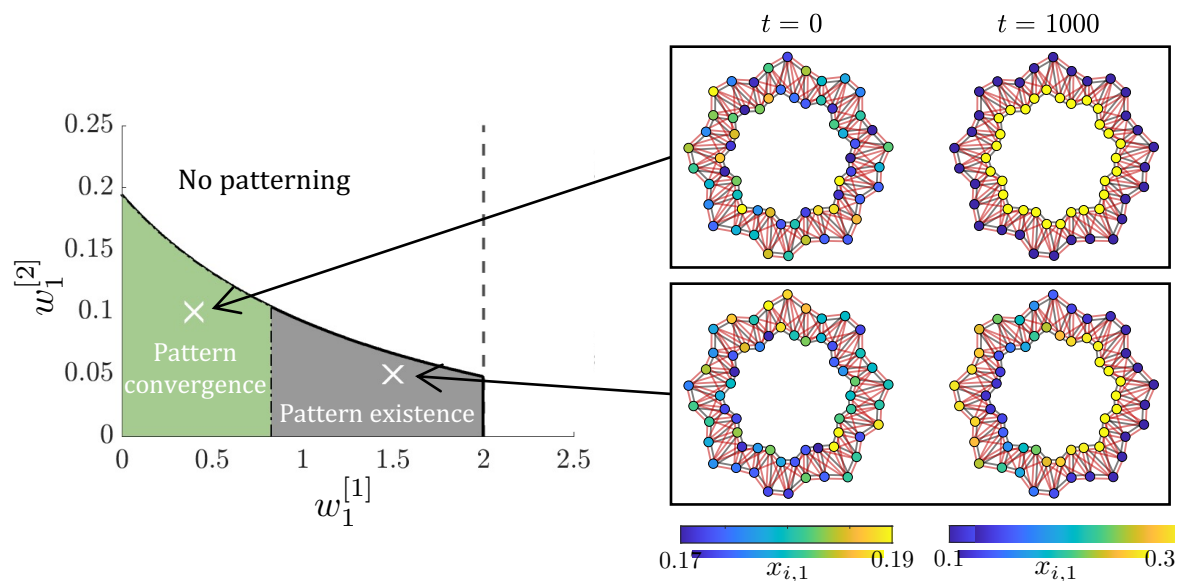


**Figure 10.** Polarity parameter regimes for the existence and convergence of laminar pattern in the large-scale IO system (3.20)–(3.24). The gray existence region is determined using the quotient system analysis and is defined by polarity-driven HSS instability inequality (3.32) for fixed  $w_2^{[1]} = w_2^{[2]} = 1$ . The green convergence region highlights the subset of the gray region in  $(w_1^{[1]}, w_1^{[2]})$ -space in which  $\min(\text{Spec}(\overline{\mathbf{W}}_k)) = \min(\text{Spec}(\mathbf{W}_k))$ . Example large-scale simulations are shown for polarity parameters inside the convergence region (0.4, 0.1) and inside the existence region (1.5, 0.05). Large-scale bilayer graphs are shown with both  $\mathcal{G}_1$  and  $\mathcal{G}_2$  embedded in the same vertex set with edges in black and red, respectively. Vertex color corresponds to the values of  $x_{i,1}$  in each  $v_i$ . Simulations were initiated from small random perturbations about the HSS of the IO system (3.20)–(3.24), and first and final states are shown following trajectory convergence. IO system (3.20)–(3.24) parameter values and details on simulations are given in Appendix B.

To highlight the results of applying both Theorems 3.5 and 3.8 to the example DIDO system (3.20)–(3.24), regions of pattern convergence were found numerically in Figure 10, which includes examples of large-scale simulations for which laminar patterns are and are not dominant. It is worth noting that the magnitude of the difference between  $w_1^{[k]}$  and  $w_2^{[k]}$  is dependent on the magnitude of the entries of  $\mathcal{DT}(\mathbf{u}_i)$  and thus assuming that  $w_1^{[k]} \ll w_2^{[k]}$  is sufficient for the monotonicity of the large-scale system but is not necessary to satisfy the type K criteria (Lemma 3.1). Subsequently, simply selecting polarity parameters in which both the HSS instability condition for the reduced system (3.32) and  $\min(\text{Spec}(\overline{\mathbf{W}}_k)) = \min(\text{Spec}(\mathbf{W}_k))$  are satisfied resulted in the large-scale system converging to laminar patterns without requiring significant layerwise polarity.

As highlighted in Example 3.2, Theorems 3.5 and 3.8 facilitate the analytic study of laminar pattern formation in large-scale interconnected dynamical systems, independent of the number of cells in the system or physical dimension due to the topological definition of the connectivity graphs. Hence, the pattern analysis conducted on the quotient systems can evolve from explorative, in which geometries enable laminar patterning, to constructive, or how much edge weight manipulation is required to robustly generate laminar patterns.

**4. Discussion.** In this study, we have developed analytic methods for exploring the interplay of cellular polarity and multiple signaling mechanisms in the emergence of laminar patterns in bilayer tissues independent of the precise intracellular kinetics. To facilitate such analysis, we focused on methods of dimension reduction of large interconnected dynamical systems that preserve fundamental cellular behavior. Specifically, we demonstrate that cell signaling transfer dynamics can be treated as a proxy for intracellular components, reducing the dimensionality of the spatially discrete ODE systems by analyzing only the spatially dependent intracellular components, which enabled us to provide sufficient conditions for the existence and uniqueness of the HSS.

In addition, we use properties of commuting graphs to decompose large MIMO systems into lower-order interconnected systems, decoupling the spatial and temporal components. This not only has advantages in reducing the computational cost associated with large-scale eigenvalue problems but also enables the direct analysis of the influence each signaling mechanism has on driving spatial instabilities of the HSS. From a practical standpoint, the requirement of commuting graphs of cell signaling currently limits the applications of the large-scale HSS instability results in general pattern formation problems, as there exist no analytically tractable methods for checking these conditions for large graphs. Therefore, developing a procedure for constructing commuting families of large signaling graphs is critical to broadening the scope of these modeling approaches.

Combining methods of multilayer graph partitions with monotone dynamical systems theory, we demonstrate that the existence of laminar pattern formation with competitive kinetics relies on the amount of signaling polarization present within each graph. Critically, the application of equitable partitions to the connectivity structures where layerwise symmetries are present enables drastic dimensionality reductions of the global dynamical system when seeking contrasting steady states between the bilayer of cells. Thereby, exploiting the spectral structure of the quotient graphs, we demonstrate the instability conditions derived for large-scale interconnected dynamical systems that can be applied to the reduced system, independent of the commutativity of the quotient graphs, which facilitates the investigation of whether the predefined contrasting states are achievable with the given kinetics. The symmetry requirements of the equitable partitions need not be restricted to globally regular cell-cell interaction graphs. We only require regularity within each partition, which therefore permits the application of semiregular graphs for dimension reduction. Such graphs can then capture characteristic traits of the biological system, such as subpopulation phenotypes and tissue curvature and their influence on intracellular behavior.

These methods of prescribing patterns allude to studying the inverse problem, specifically, starting with the desired pattern of the tissue and then defining constraints for the intracellular kinetics that have the potential to induce such instabilities, as previously demonstrated in spatially continuous Turing systems [68]. Additionally, as the full and quotient system analysis depends only on the topology of the connectivity networks, the results from this study are immediately applicable to more biologically relevant three-dimensional morphologies. Classically, introducing three-dimensional structures drastically increases the computational complexity in pattern formation analysis [8, 39, 50], yet the topological approach allows for the transition between physical dimension with no additional requirements, as discussed in [45].

Investigating the link between the reduced and large-scale dynamical systems when seeking laminar patterns, we demonstrate that the statements of laminar existence, derived using pattern templating, have the capacity to be globally convergent in the corresponding large-scale interconnected system in high-polarity regimes. To show the existence of a monotone transformation, we imposed weak but sufficient conditions that  $w_1^{[k]} \ll w_2^{[k]}$ , highlighting the requirement of edge weight anisotropy for laminar pattern formation. However, we suspect that this condition can be significantly refined by illustrating a dependence on the magnitude of entries of  $\mathcal{DT}(\mathbf{u}_i)$  when applying the type K criterion for monotone solution behavior, namely, having a priori estimations of the size of the cellular output signals for given input signal regimes.

Furthermore, to explore these links between the quotient and large-scale systems, we impose the restrictive semiregular bilayer structure with identical edge weights. This ensures the existence of an equitable partition to generate low-dimensional dynamical representations with common spectra which is guided by a graphical perspective. However, these vertex symmetries are not the only method of preserving the spectra between quotient and large-scale systems. These results may be generalized to less restrictive spatial domains which are more realistic in biological applications by investigating the lifting maps of the pattern representing quotient graphs, as previously considered in synchronized subspaces of balanced systems [2]. In addition, our methods of ensuring desired pattern convergence in the large-scale dynamics by exploiting the simple block structure of the weighted adjacency matrices  $\mathbf{W}_k \in \mathcal{W}$  can also be generalized by the row-sum constructions of block weighted adjacency matrices in general liftings, as highlighted in [2, 3], such that the structures considered in this study present a special case of those discussed previously. Subsequently, further work is required to isolate desired vertex pattern modes from generic lifted weighted adjacency matrices, specifically under the control of edge weights, to satisfy the type K criterion to guarantee global convergence within these more general graph structures.

As discussed in the previous interconnected monotone systems studies of pattern formation [7, 25, 26], the most limiting assumption in large-scale systems analysis is the existence of competitive-to-cooperative monotone kinetics transformation, which previously has relied on the sufficient requirement of the connectivity graphs being bipartite. However, in section 3.4, we demonstrate not only that laminar patterns are not the dominant pattern of bipartite bilayer graphs but also that manipulating graph edge weights of nonbipartite graphs enables competitive-to-cooperative kinetics transformations for laminar pattern formation. The key feature of cooperative dynamics used in these pattern formation studies is the guarantee of nonperiodic solutions when considering bounded kinetics [57]. Therefore, another promising direction to ensure such solution behavior is the study of variational families associated with the interconnected systems [5], that is, applying Lyapunov methods for nonoscillatory dynamics to enable the investigation of intracellular crosstalk inference in biologically relevant morphologies.

Throughout this study, we have reserved the precise definitions of the intracellular kinetics and associated signaling mechanisms to consider general competitive MIMO dynamics. Subsequently, the generality of results presented here enables the investigation of crosstalk of key molecular pathways with multiple spatially dependent intracellular signaling components,

such as the well-established Wnt-Notch interactions that have been observed in both intestinal and mammary epithelia [17]. Both the Wnt and Notch pathways are involved in cell-fate determination and have been observed to have active apical-basal polarity mechanisms during tissue development [10, 55]. However, existing models have previously been limited to analysis of one or two cells [4, 37]. The methods we provide here allow us to study how the geometry of the tissue influences such cell-fate choices, specifically within the bilayer structures commonly found in mammary glands.

**Appendix A. Additional properties of interwoven matrices.** Here, we present further properties of interwoven matrices which have particular applications in dynamical network theory of mixed kernels. Specifically, an interwoven matrix  $\mathbf{P}$  is composed of the sequence of real matrices  $\mathcal{M} = \{M_i \mid M_i \in \mathbb{R}^{N \times N}\}$  called constructor matrices such that the rows and columns of each matrix  $M_i$  are uniformly separated by zero elements, preserving the structure of  $M_i$ , where the order of  $\mathcal{M}$  defines the sequence of spacing. Formally, we define an interwoven matrix  $\mathbf{P}$  by

$$(A.1) \quad \mathbf{P} = \sum_{i=1}^r M_i \otimes \text{diag}(\delta_{i,1}, \dots, \delta_{i,r}),$$

where  $\otimes$  is the Kronecker product and  $\delta_{i,j}$  is the Kronecker delta function (2.4) as defined in section 2.1. Here we do not assume that the constructor matrices  $M_i$  are nonnegative.

The following statement provides a constructive diagonal decomposition of the  $\mathbf{P}$ , illuminating the spectral structure of  $\mathbf{P}$ .

**Lemma A.1.** *Let  $\mathbf{P}$  be the interwoven matrix defined as defined in (A.1), and let  $\mathbf{Q}$  be the permutation matrix such that*

$$(A.2) \quad \mathbf{Q} = [\mathbf{I}_N \otimes \mathbf{e}_1, \dots, \mathbf{I}_N \otimes \mathbf{e}_r].$$

where  $\mathbf{e}_i = [\delta_{i,1}, \dots, \delta_{i,r}]^T$ . Then

$$(A.3) \quad \mathbf{Q}^T \mathbf{P} \mathbf{Q} = \bigoplus_{i=1}^r M_i,$$

where  $\bigoplus$  is the direct sum of tensors.

*Proof.* Consider the permutation map  $\tau: \{1, \dots, rN\} \rightarrow \{1, \dots, rN\}$  such that

$$(A.4) \quad \tau(x) = ((x-1) \bmod r)N + \left\lfloor \frac{x-1}{r} \right\rfloor + 1,$$

which permutes the rows and columns of  $\mathbf{P}$  so that any row and columns  $M_i$  of  $\mathbf{P}$  become adjacent for  $1 \leq i \leq r$ . In cycle notation,  $\tau(x)$  defines the mapping

$$(A.5) \quad \begin{pmatrix} 1 & 2 & \dots & r & r+1 & \dots & rN \\ 1 & N+1 & \dots & (r-1)N+1 & 2 & \dots & (r-1)N+N \end{pmatrix},$$

which represents the column and row permutation of  $\mathbf{P}$ . The cycle (A.5) defined by (A.4) yields the matrix representation

$$(A.6) \quad \mathbf{Q} = [\mathbf{I}_N \otimes \mathbf{e}_1, \dots, \mathbf{I}_N \otimes \mathbf{e}_r];$$

namely,  $Q_{i,\tau(i)} = 1$  and zero entries else. Therefore, applying the transformation  $\mathbf{Q}$  to  $\mathbf{P}$  produces the block diagonal representation where

$$(A.7) \quad \mathbf{Q}^T \mathbf{P} \mathbf{Q} = \text{blkdiag}(\mathbf{M}_1, \dots, \mathbf{M}_r),$$

which is by definition the direct sum of matrices  $\mathbf{M}_i$ . ■

The block diagonal representation of  $\mathbf{P}$  following from (A.3) motivates the subsequent properties involving the spectra and inverse of the interwoven matrix  $\mathbf{P}$ .

**Lemma A.2.** *Let  $\mathbf{P}$  be the interwoven matrix as defined in (A.1). Then  $\mathbf{P}$  has the following properties:*

(i)

$$(A.8) \quad \text{Spec}(\mathbf{P}) = \bigcup_{i=1}^r \text{Spec}(\mathbf{M}_i)$$

*including multiplicities.*

(ii) *If  $\mathbf{M}_i$  is invertible for all  $1 \leq i \leq k$ , then the inverse of the interwoven matrix  $\mathbf{P}$  is the interweave of the inverse of the constructor matrices. That is,*

$$(A.9) \quad \mathbf{P}^{-1} = \sum_{i=1}^r \mathbf{M}_i^{-1} \otimes \text{diag}(\delta_{i,1}, \dots, \delta_{i,r}).$$

(iii) *The trace of the interwoven matrix is the sum of the traces of the constructor matrices*

$$(A.10) \quad \text{tr}(\mathbf{P}) = \sum_{i=1}^r \text{tr}(\mathbf{M}_i).$$

(iv) *The determinant of the interwoven matrix is the product of the determinant of the constructor matrices*

$$(A.11) \quad \det(\mathbf{P}) = \prod_{i=1}^r \det(\mathbf{M}_i).$$

**Proof.** Let  $\lambda_{k,j} \in \text{Spec}(\mathbf{M}_k)$  with its associated eigenvector  $\mathbf{v}_{k,j}$ . Then define the interweave extension of  $\mathbf{v}_{k,j}$  by

$$(A.12) \quad \tilde{\mathbf{v}}_{k,j} = \mathbf{v}_{k,j} \otimes \begin{bmatrix} \delta_{k,1} \\ \vdots \\ \delta_{k,r} \end{bmatrix}.$$

For brevity, denote the Kronecker diagonal matrix by  $\mathbf{D}_i = \text{diag}(\delta_{i,1}, \dots, \delta_{i,r})$ , and then by direct computation, we have

$$\begin{aligned}
 \mathbf{P}\tilde{\mathbf{v}}_{k,j} &= \left( \sum_{i=1}^r \mathbf{M}_i \otimes \mathbf{D}_i \right) \tilde{\mathbf{v}}_{k,j}, \\
 &= \left( \sum_{i=1}^r \mathbf{M}_i \otimes \mathbf{D}_i \right) \left( \mathbf{v}_{k,j} \otimes [\delta_{k,1}, \dots, \delta_{k,r}]^T \right), \\
 &= \left( \sum_{i=1}^r \mathbf{M}_i \mathbf{v}_{k,j} \otimes \mathbf{D}_i [\delta_{k,1}, \dots, \delta_{k,r}]^T \right), \\
 \text{(A.13)} \quad &= \mathbf{M}_k \mathbf{v}_{k,j} \otimes [\delta_{k,1}, \dots, \delta_{k,r}]^T,
 \end{aligned}$$

where the last two equalities follow from the mixed-product property of the Kronecker product and the direct multiplication of the Kronecker matrix and vector are nonzero only if  $i = j$ . Therefore, we have that

$$\text{(A.14)} \quad \mathbf{P}\tilde{\mathbf{v}}_{k,j} = \mathbf{M}_k \mathbf{v}_{k,j} \otimes [\delta_{k,1}, \dots, \delta_{k,r}]^T = \lambda_{k,j} \mathbf{v}_{k,j} \otimes [\delta_{k,1}, \dots, \delta_{k,r}]^T = \lambda_{k,j} \tilde{\mathbf{v}}_{k,j};$$

thus,  $\lambda_{k,j}$  is an eigenvalue of  $\mathbf{P}$  with associated eigenvector  $\tilde{\mathbf{v}}_{k,j}$ .

Next, there exists  $\mathbf{M}_i^{-1}$  for all  $1 \leq i \leq r$  from the assumption in (ii). Note that

$$\text{(A.15)} \quad \mathbf{D}_i \mathbf{D}_j = \begin{cases} \mathbf{D}_i & i = j, \\ \mathbf{0}_{r \times r} & i \neq j. \end{cases}$$

Then consider the following matrix  $\mathbf{R}$  defined by the multiplication:

$$\begin{aligned}
 \mathbf{R} &= \left( \sum_{i=1}^r \mathbf{M}_i \otimes \mathbf{D}_i \right) \left( \sum_{i=1}^r \mathbf{M}_i^{-1} \otimes \mathbf{D}_i \right), \\
 \text{(A.16)} \quad &= (\mathbf{M}_1 \otimes \mathbf{D}_1) \left( \sum_{i=1}^r \mathbf{M}_i^{-1} \otimes \mathbf{D}_i \right) + \dots + (\mathbf{M}_r \otimes \mathbf{D}_r) \left( \sum_{i=1}^r \mathbf{M}_i^{-1} \otimes \mathbf{D}_i \right).
 \end{aligned}$$

From the mixed-product property of the Kronecker product and equation (A.15), we have that (A.16) reduces to

$$\begin{aligned}
 \mathbf{R} &= \mathbf{M}_1 \mathbf{M}_1^{-1} \otimes \mathbf{D}_1 + \dots + \mathbf{M}_r \mathbf{M}_r^{-1} \otimes \mathbf{D}_r, \\
 \text{(A.17)} \quad &= \sum_{i=1}^r \mathbf{I}_n \otimes \mathbf{D}_i = \mathbf{I}_{rN}.
 \end{aligned}$$

Hence, the inverse of  $\mathbf{P}$  is given by  $\mathbf{P}^{-1} = \sum_{i=1}^r \mathbf{M}_i^{-1} \otimes \mathbf{D}_i$  as required for (ii).

The trace of a Kronecker product is the product of the trace [27] such that  $\text{tr}(\mathbf{M}_i \otimes \mathbf{D}_i) = \text{tr}(\mathbf{M}_i) \text{tr}(\mathbf{D}_i)$ . Therefore, applying the trace to the definition of  $\mathbf{P}$  (A.1) yields

$$(A.18) \quad \text{tr}(\mathbf{P}) = \text{tr}\left(\sum_{i=1}^r \mathbf{M}_i \otimes \mathbf{D}_i\right) = \sum_{i=1}^r \text{tr}(\mathbf{M}_i \otimes \mathbf{D}_i) = \sum_{i=1}^r \text{tr}(\mathbf{M}_i) \text{tr}(\mathbf{D}_i) = \sum_{i=1}^r \text{tr}(\mathbf{M}_i),$$

where the second equality holds by the trace of the sum of matrices [27] and the fourth holds by  $\text{tr}(\mathbf{D}_i) = 1$  for all  $1 \leq i \leq r$ .

Property (iv) follows immediately from (i) by expressing the determinant of a matrix as the product of the eigenvalues including multiplicities [27]. From (i), we have that  $\text{Spec}(\mathbf{P}) = \text{Spec}(\mathbf{M}_1) \cup \dots \cup \text{Spec}(\mathbf{M}_r)$  including multiplicities, and so we know that the eigenvalues of  $\mathbf{P}$  are all the eigenvalues of each  $\mathbf{M}_i$ . Subsequently, the determinant of  $\mathbf{P}$  must be the product of all these eigenvalues which leads to the required representation

$$(A.19) \quad \det(\mathbf{P}) = \left(\prod_{j=1}^N \lambda_{1,j}\right) \dots \left(\prod_{j=1}^N \lambda_{r,j}\right) = \det(\mathbf{M}_1) \dots \det(\mathbf{M}_r) = \prod_{i=1}^r \det(\mathbf{M}_i). \quad \blacksquare$$

A direct consequence of Theorem A.2 is that if  $\mathbf{M}_j$  are nonnegative, then the spectral radius,  $\rho$ , of interwoven matrix  $\mathbf{P}$  is a real eigenvalue and is defined by

$$(A.20) \quad \rho(\mathbf{P}) = \max_i (\rho(\mathbf{M}_i)) = \max\left(\bigcup_{i=1}^r \text{Spec}(\mathbf{M}_i)\right)$$

from the Perron–Frobenius theorem for nonnegative matrices [57].

In addition to its spectral properties, the interwoven matrix (A.1) also has the following exponent property.

**Lemma A.3.** *Let  $\mathbf{P}$  be the interwoven matrix defined as defined in (A.1). Then for all  $n \in \mathbb{N}$ ,*

$$(A.21) \quad \mathbf{P}^n = \sum_{i=1}^r \mathbf{M}_i^n \otimes \mathbf{D}_i.$$

*Proof.* The result follows by induction. Assume for some  $k \in \mathbb{N}$  that (A.21) holds. Consider the case for  $k + 1$ ,

$$(A.22) \quad \begin{aligned} \left(\sum_{i=1}^r \mathbf{M}_i \otimes \mathbf{D}_i\right)^{k+1} &= \left(\sum_{i=1}^r \mathbf{M}_i \otimes \mathbf{D}_i\right) \left(\sum_{i=1}^r \mathbf{M}_i \otimes \mathbf{D}_i\right)^k, \\ &= \left(\sum_{i=1}^r \mathbf{M}_i \otimes \mathbf{D}_i\right) \left(\sum_{i=1}^r \mathbf{M}_i^k \otimes \mathbf{D}_i\right), \end{aligned}$$

where the second equality follows from the inductive hypothesis. Applying the multiplication property of the Kronecker matrix equation (A.15), expansion of (A.22), and the mixed-product property of the Kronecker product leads to the following cancellations:

$$\begin{aligned}
 & \left( \sum_{i=1}^r M_i \otimes D_i \right) \left( \sum_{i=1}^r M_i^k \otimes D_i \right) \\
 &= (M_1 \otimes D_1) \left( \sum_{i=1}^r M_i^k \otimes D_i \right) + \cdots + (M_r \otimes D_r) \left( \sum_{i=1}^r M_i^k \otimes D_i \right), \\
 &= M_1 M_1^k \otimes D_1 + \cdots + M_r M_r^k \otimes D_r, \\
 \text{(A.23)} \quad &= \sum_{i=1}^r M_i^{k+1} \otimes D_i.
 \end{aligned}$$

That is, the inductive hypothesis is satisfied, and thus (A.21) holds for all  $n \in \mathbb{N}$  by the principle of induction.  $\blacksquare$

**Appendix B. Computational methods.** The ODE systems in this study were solved numerically using the `ODE15s` solver in MATLAB (R2021a). Simulations were performed over a total of 1000 time units in addition to a stopping event applied to the ODE solver to check for solution convergence. Namely, if all trajectories varied less than  $1 \times 10^{-4}$  over four consecutive iterations, then we assume that the system has converged to a steady state. We note that all simulations presented in this study satisfied the convergence criteria. The intracellular kinetics parameter values of the IO system (3.20–3.24) used in all simulations are given in Table 1.

Random initial conditions were sampled from a uniform distribution using the `rand` function. The HSS of the system was calculated using the `fsolve` function, which implements the trust-region-dogleg minimization algorithm [15]. In addition, heterotypic weighting parameters was set to  $w_2^{[k]} = 1$  for all simulations. Both quotient and large-scale ODE systems were solved using the same kinetics functions where respective adjacency matrices were introduced as an argument to these kinetics functions to ensure solution consistency.

To visualize the approximate cell membranes in the large-scale simulation, Voronoi diagrams were drawn around graph vertices using the `delaunayTriangulation` and `voronoi` functions within the Computational Geometry toolbox in MATLAB (R2021a). Ghost vertices were introduced to ensure that each graph vertex has a closed boundary.

Eigenvalues of the adjacency matrices were calculated using the `eig` function from the Linear Algebra toolbox in MATLAB (R2021a). The edge structures of the semiregular nonbipartite graphs used in the numerical spectral investigation are given in Table 2. These graphs were confirmed nonbipartite by violating the spectral symmetry property of bipartite graphs.

**Table 1**

*Parameter values used in the simulations of the IO system (3.20)–(3.24).*

Parameter	$a_1$	$a_2$	$b_1$	$b_2$	$b_3$	$k_1$	$k_2$	$h_1$	$h_2$	$h_3$
Value	0.01	1	100	100	100	2	2	2	2	1

Table 2

Summary of the bilayer edge connectivity structures for the graphs used in the numerical investigation of nonbipartite spectra in Figure 9.

	$n_{1,\mathcal{L}_1}$	$n_{2,\mathcal{L}_1}$	$n_{1,\mathcal{L}_2}$	$n_{2,\mathcal{L}_2}$
$\mathcal{G}_1$	2	2	2	2
$\mathcal{G}_2$	2	3	2	3
$\mathcal{G}_3$	2	4	2	4
$\mathcal{G}_4$	4	3	4	3

Source code for the simulations presented in this study can be found at [https://github.com/joshwillmoore1/Mixed\\_Signal\\_mechanisms](https://github.com/joshwillmoore1/Mixed_Signal_mechanisms).

**Appendix C. Proof of  $\pi_2$ -dependent spectral gap for  $\mathcal{G}_{2D}$  and  $\mathcal{G}_{3D}$  from Figure 8(B).**

Bipartite graphs have many particularly convenient algebraic properties due to the existence of a simple canonical form of the respective adjacency matrix. Namely, for any bipartite graph  $\mathcal{G}_k$  with adjacency matrix  $\mathbf{W}_k$ , there exists a permutation matrix  $\mathbf{U}$  that reindexes the vertices with respect to the independent sets  $V_1$  and  $V_2$  such that

$$(C.1) \quad \mathbf{U}^T \mathbf{W}_k \mathbf{U} = \begin{bmatrix} \mathbf{0} & \mathbf{X}_k \\ \mathbf{X}_k^T & \mathbf{0} \end{bmatrix},$$

where  $\mathbf{X}_k$  is the biadjacency matrix [20]. Subsequently, the spectra of the bipartite graphs have a distinct structure such that there is a symmetry of eigenvalues respective to the biadjacency matrices, i.e.,  $\text{Spec}(\mathbf{W}_k) = \text{Spec}(\mathbf{X}_k) \cup \text{Spec}(-\mathbf{X}_k)$ . Leveraging the spectral symmetry of bipartite graphs and the spectral retention of equitable partitions, we demonstrate that for the bipartite bilayer graphs  $\mathcal{G}_{2D}$  and  $\mathcal{G}_{3D}$  in Figure 8, the smallest eigenvalue of  $\mathbf{X}_k$  is  $-\bar{\lambda}_{k,2}$ , the polarity-driven eigenvalue associated with laminar pattern template  $\pi_2$ .

**Lemma C.1.** *Let  $\mathcal{G}_k$  be a regular bipartite bilayer graph with associated row-stochastic weighted adjacency matrix  $\mathbf{W}_k$  (2.8) for two- or three-dimensional tissues, as shown in Figure 8 ( $k = 2D, 3D$ ). Consider the equitable partition  $\pi_2$  such that the quotient graph,  $\mathcal{G}_{k,\pi_2}$ , consists of only two representative vertices in each layer of  $\mathcal{G}_k$  and has the reduced adjacency matrix  $\bar{\mathbf{W}}_k$  (3.5). Then biadjacency matrix  $\mathbf{X}_k$  associated with  $\mathbf{W}_k$  satisfies*

$$(C.2) \quad -\bar{\lambda}_{k,2} = \min(\text{Spec}(\mathbf{X}_k)),$$

where  $\bar{\lambda}_{k,2}$  is the smallest eigenvalue of  $\bar{\mathbf{W}}_k$  with associated eigenvector  $\bar{\mathbf{v}}_{k,2}$ .

*Proof.* We present the proof for  $\mathcal{G}_{2D}$ , as the following argument holds immediately for  $\mathcal{G}_{3D}$  also. As we make use of the biadjacency form of  $\mathbf{W}_{2D}$ , we first construct the biadjacency transformation  $\mathbf{U}$ . The bipartite bilayer graph  $\mathcal{G}_{2D}$  has vertex indices in layerwise order as defined in section 2.1 with block adjacency matrices given in Example 2.2. To reorder the vertices of  $\mathcal{G}_{2D}$  such that vertex groups  $V_1$  and  $V_2$  are ordered consecutively, we define the permutation matrix

$$(C.3) \quad \mathbf{U} = \begin{bmatrix} \mathbf{I}_{|\mathcal{L}_1|/2} \otimes \mathbf{D}_1 & \mathbf{I}_{|\mathcal{L}_1|/2} \otimes \mathbf{D}_2 \\ \mathbf{I}_{|\mathcal{L}_2|/2} \otimes \mathbf{D}_2 & \mathbf{I}_{|\mathcal{L}_2|/2} \otimes \mathbf{D}_1 \end{bmatrix},$$

where  $|\mathcal{L}_1| = |\mathcal{L}_2|$ , as each layer has the same number of vertices. In particular, we have the biadjacency form

$$(C.4) \quad \begin{aligned} U^T \mathbf{W}_{2D} U &= \begin{bmatrix} \mathbf{I}_{|\mathcal{L}_1|/2} \otimes \mathbf{D}_1 & \mathbf{I}_{|\mathcal{L}_1|/2} \otimes \mathbf{D}_2 \\ \mathbf{I}_{|\mathcal{L}_2|/2} \otimes \mathbf{D}_2 & \mathbf{I}_{|\mathcal{L}_2|/2} \otimes \mathbf{D}_1 \end{bmatrix} \begin{bmatrix} \widehat{\mathbf{W}}_{1,\mathcal{L}_1} & \widehat{\mathbf{W}}_{2,\mathcal{L}_1} \\ \widehat{\mathbf{W}}_{2,\mathcal{L}_1}^T & \widehat{\mathbf{W}}_{1,\mathcal{L}_2} \end{bmatrix} \begin{bmatrix} \mathbf{I}_{|\mathcal{L}_1|/2} \otimes \mathbf{D}_1 & \mathbf{I}_{|\mathcal{L}_1|/2} \otimes \mathbf{D}_2 \\ \mathbf{I}_{|\mathcal{L}_2|/2} \otimes \mathbf{D}_2 & \mathbf{I}_{|\mathcal{L}_2|/2} \otimes \mathbf{D}_1 \end{bmatrix} \\ &= \begin{bmatrix} 0 & \mathbf{X}_{2D} \\ \mathbf{X}_{2D} & 0 \end{bmatrix} \end{aligned}$$

for  $\mathbf{X}_{2D}$  in cyclic tridiagonal form

$$(C.5) \quad \mathbf{X}_{2D} = \begin{bmatrix} \hat{w}_2^{[2D]} & \hat{w}_1^{[2D]} & 0 & \cdots & 0 & \hat{w}_1^{[2D]} \\ \hat{w}_1^{[2D]} & \hat{w}_2^{[2D]} & \hat{w}_1^{[2D]} & & & \\ & & \ddots & & & \\ & & & \ddots & & \\ & & & & \hat{w}_1^{[2D]} & \hat{w}_2^{[2D]} & \hat{w}_1^{[2D]} \\ \hat{w}_1^{[2D]} & 0 & \cdots & 0 & \hat{w}_1^{[2D]} & \hat{w}_2^{[2D]} \end{bmatrix},$$

noting that  $\mathbf{X}_{2D}^T = \mathbf{X}_{2D}$  by the regularity of  $\mathcal{G}_{2D}$ , and therefore  $U^T \mathbf{W}_{2D} U$  is symmetric.

As the laminar pattern template partition  $\pi_2$  is equitable, there exists a lifting matrix  $\mathbf{L} \in \{0, 1\}^{N \times 2}$  that maps the large-scale adjacency matrix  $\mathbf{W}_{2D}$  into its reduced form  $\overline{\mathbf{W}}_{2D}$  such that

$$(C.6) \quad \mathbf{W}_{2D} \mathbf{L} = \mathbf{L} \overline{\mathbf{W}}_{2D},$$

as demonstrated in [21]. The lifting transformation is constructed by grouping vertices associated with the partition  $\pi_2$  on  $\mathbf{W}_{2D}$ ; for example,  $L_{ij} = 1$  if  $v_i \in \mathcal{L}_j$ . Due to the block structure of  $\mathbf{W}_{2D}$  (2.8) which follows from the layerwise vertex indexing, we have that

$$(C.7) \quad \mathbf{L} = \begin{bmatrix} \mathbf{1}_{|\mathcal{L}_1|,1} & \mathbf{0}_{|\mathcal{L}_1|,1} \\ \mathbf{0}_{|\mathcal{L}_2|,1} & \mathbf{1}_{|\mathcal{L}_2|,1} \end{bmatrix}.$$

Critically, the lifting matrix  $\mathbf{L}$  provides the algebraic link between the quotient and large-scale graphs.

Following from the regular structure of  $\mathcal{G}_{2D}$  and direct computation, the eigenvector associated with  $\bar{\lambda}_{2D,2}$  has the form  $\bar{\mathbf{v}}_{2D,2} = [1, -1]^T$ . The spectral retention property of the equitable partition,  $\pi_2$ , guarantees that  $\bar{\lambda}_{2D,2} \in \text{Spec}(\mathbf{W}_{2D})$ , where  $\mathbf{L} \bar{\mathbf{v}}_{2D,2}$  is the corresponding eigenvector for the large-scale graph  $\mathcal{G}_{2D}$  (by Theorem 9.3.3 of [20]). Explicitly, we have that the lifted eigenvector is of the form

$$(C.8) \quad \mathbf{L} \bar{\mathbf{v}}_{2D,2} = \begin{bmatrix} \mathbf{1}_{|\mathcal{L}_1|,1} \\ -\mathbf{1}_{|\mathcal{L}_2|,1} \end{bmatrix},$$

with associated eigenvalue  $\bar{\lambda}_{2D,2}$ . In the biadjacency matrix form (C.4), the corresponding eigenvector has the transformed representation

$$(C.9) \quad \boldsymbol{\nu} := U^T \mathbf{L} \bar{\mathbf{v}}_{2D,2} = \underbrace{[1 \quad -1 \quad \cdots \quad 1 \quad -1]}_{|\mathcal{L}_1|} \underbrace{[1 \quad -1 \quad \cdots \quad 1 \quad -1]}_{|\mathcal{L}_2|}^T.$$

The spectral symmetry of bipartite graphs ensures that if there exists an eigenpair  $(\bar{\lambda}_{2D,2}, \boldsymbol{\nu} = [\mathbf{x}, \mathbf{y}^T])$ , then there must also exist the eigenpair  $(-\bar{\lambda}_{2D,2}, \tilde{\boldsymbol{\nu}} = [\mathbf{x}, -\mathbf{y}^T])$  [20]. Therefore, the eigenvector associated with  $-\lambda_{2D,2}$  has biadjacency form

$$(C.10) \quad \tilde{\boldsymbol{\nu}} = \underbrace{[1 \quad -1 \quad \cdots \quad 1 \quad -1]}_{|\mathcal{L}_1|} \underbrace{[-1 \quad 1 \quad \cdots \quad -1 \quad 1]}_{|\mathcal{L}_2|}^T,$$

which negates the signs of those entries associated with the latter half of the vertices in  $\mathcal{G}_{2D}$ . Subsequently, the first  $|\mathcal{L}_1|$  entries of  $\tilde{\boldsymbol{\nu}}$  are an eigenvector of  $\mathbf{X}_{2D}$  with eigenvalue  $-\bar{\lambda}_{2D,2}$  following from the canonical biadjacency representation of  $\mathbf{W}_{2D}$  (C.4). We denote this reduced eigenvector in normalized form as

$$(C.11) \quad \tilde{\boldsymbol{\nu}}_1 = \frac{1}{\sqrt{|\mathcal{L}_1|}} \underbrace{[1 \quad -1 \quad \cdots \quad 1 \quad -1]}_{|\mathcal{L}_1|}^T,$$

and therefore it remains to show that the eigenpair  $(-\bar{\lambda}_{2D,2}, \tilde{\boldsymbol{\nu}}_1)$  is minimal in the spectrum of  $\mathbf{X}_{2D}$ .

The Rayleigh quotient for  $\mathbf{X}_{2D}$  is defined by

$$(C.12) \quad R_{\mathbf{X}_{2D}}(\mathbf{y}) = \frac{\mathbf{y}^T \mathbf{X}_{2D} \mathbf{y}}{\mathbf{y}^T \mathbf{y}},$$

and as  $\mathbf{X}_{2D}$  is real and symmetric by the min-max theorem, the Rayleigh quotient is bounded by the maximal and minimal eigenvalues of the matrix,  $R_{\mathbf{X}_{2D}}(\mathbf{y}) \in [\lambda_{\min}, \lambda_{\max}]$  [20]. In particular,  $R_{\mathbf{X}_{2D}}(\mathbf{y})$  generates the eigenvalues of  $\mathbf{X}_{2D}$  when  $\mathbf{y}$  is the respective eigenvector. Hence, we show that  $\tilde{\boldsymbol{\nu}}_1$  minimizes  $R_{\mathbf{X}_{2D}}(\mathbf{y})$ , namely,

$$(C.13) \quad \arg \min_{\substack{\mathbf{y} \in \mathbb{R}^{|\mathcal{L}_1|} \\ \|\mathbf{y}\|=1}} (R_{\mathbf{X}_{2D}}(\mathbf{y})) = \tilde{\boldsymbol{\nu}}_1,$$

where the normality constraint follows from  $\mathbf{X}_{2D}$  being real and symmetric, and so the eigenvectors of  $\mathbf{X}_{2D}$  are orthonormal with real eigenvalues.

The normalized form of  $\tilde{\boldsymbol{\nu}}_1$  yields  $\tilde{\boldsymbol{\nu}}_1^T \tilde{\boldsymbol{\nu}}_1 = 1$ , and therefore the Rayleigh quotient evaluated at  $\tilde{\boldsymbol{\nu}}_1$  simplifies to  $R_{\mathbf{X}_{2D}}(\tilde{\boldsymbol{\nu}}_1) = \tilde{\boldsymbol{\nu}}_1^T \mathbf{W}_{2D} \tilde{\boldsymbol{\nu}}_1$ . By direct computation, we have that

$$(C.14) \quad \begin{aligned} \tilde{\boldsymbol{\nu}}_1^T \mathbf{X}_{2D} \tilde{\boldsymbol{\nu}}_1 &= \sum_{k=1}^{|\mathcal{L}_1|} \sum_{j=1}^{|\mathcal{L}_1|} (\mathbf{X}_{2D})_{k,j} (\tilde{\boldsymbol{\nu}}_1)_k (\tilde{\boldsymbol{\nu}}_1)_j \\ &= \sum_{i=1}^{|\mathcal{L}_1|} (\mathbf{X}_{2D})_{ii} (\tilde{\boldsymbol{\nu}}_1)_i^2 + \sum_{i=2}^{|\mathcal{L}_1|-1} (\tilde{\boldsymbol{\nu}}_1)_i \left( (\mathbf{X}_{2D})_{i,i-1} (\tilde{\boldsymbol{\nu}}_1)_{i-1} + (\mathbf{X}_{2D})_{i,i+1} (\tilde{\boldsymbol{\nu}}_1)_{i+1} \right) \\ &\quad + (\tilde{\boldsymbol{\nu}}_1)_1 \left( (\mathbf{X}_{2D})_{1,2} (\tilde{\boldsymbol{\nu}}_1)_2 + (\mathbf{X}_{2D})_{1,|\mathcal{L}_1|} (\tilde{\boldsymbol{\nu}}_1)_{|\mathcal{L}_1|} \right) \\ &\quad + (\tilde{\boldsymbol{\nu}}_1)_{|\mathcal{L}_1|} \left( (\mathbf{X}_{2D})_{|\mathcal{L}_1|,1} (\tilde{\boldsymbol{\nu}}_1)_1 + (\mathbf{X}_{2D})_{|\mathcal{L}_1|,|\mathcal{L}_1|-1} (\tilde{\boldsymbol{\nu}}_1)_{|\mathcal{L}_1|-1} \right) \end{aligned}$$

by the cyclic tridiagonal form of  $\mathbf{X}_{2D}$  (C.5). Critically, as  $(\mathbf{X}_{2D})_{i,j} \geq 0$  for all  $i, j$ ,  $\tilde{\boldsymbol{\nu}}_1^T \mathbf{X}_{2D} \tilde{\boldsymbol{\nu}}_1$  is minimized when  $\text{Sgn}((\tilde{\boldsymbol{\nu}}_1)_k) \neq \text{Sgn}((\tilde{\boldsymbol{\nu}}_1)_{k+1})$  for all  $k \in \{1, \dots, |\mathcal{L}_1| - 1\}$ , which is satisfied

by definition of  $\tilde{\nu}_1$ . Furthermore, the orthonormal property of the eigenbasis of  $\mathbf{X}_{2D}$  ensures that no other eigenvector has this alternating sign structure, which implies that  $-\bar{\lambda}_{2D,2}$  is the smallest eigenvalue of  $\mathbf{X}_{2D}$ . ■

A consequence of Lemma C.1 is the existence of a spectral gap about the origin for  $\mathcal{G}_{2D}$  and  $\mathcal{G}_{3D}$ .

**Theorem C.2.** *Let  $\mathcal{G}_k$  and  $\mathcal{G}_{k,\pi_2}$  be defined as in Lemma C.1, and let  $\lambda_{k,j} \in \text{Spec}(\mathbf{W}_k)$ . If  $\bar{\lambda}_{k,2} < 0$ , then  $\lambda_{k,j} \notin (\bar{\lambda}_{k,2}, -\bar{\lambda}_{k,2})$ .*

*Proof.* From Lemma C.1, we have that  $-\bar{\lambda}_{k,2} = \min(\mu_{k,j} : \mu_{k,j} \in \text{Spec}(\mathbf{X}_k))$ , and thus  $-\bar{\lambda}_{k,2} > 0$ . From the symmetry of the spectrum of bipartite graphs, we have that  $\bar{\lambda}_{k,2} < 0$  is the maximum of the negative eigenvalues of  $\mathbf{W}_k$ , therefore defining a region about the origin bounded by  $\bar{\lambda}_{k,2}$  and  $-\bar{\lambda}_{k,2}$  that contains no eigenvalues. ■

## REFERENCES

- [1] P. AGARWAL, M. JLELI, AND B. SAMET, *Banach contraction principle and applications*, in Fixed Point Theory in Metric Spaces, Springer-Verlag, Berlin, 2018, pp. 1–23.
- [2] M. A. AGUIAR AND A. P. S. DIAS, *Synchronization and equitable partitions in weighted networks*, Chaos, 28 (2018), 073105.
- [3] M. A. AGUIAR, A. P. S. DIAS, AND H. RUAN, *Synchrony patterns in gene regulatory networks*, Phys. D, 429 (2022), 133065.
- [4] Z. AGUR, O. U. KIRNASOVSKY, G. VASSERMAN, L. TENCER-HERSHKOWICZ, Y. KOGAN, H. HARRISON, R. LAMB, AND R. B. CLARKE, *Dickkopf1 regulates fate decision and drives breast cancer stem cells to differentiation: An experimentally supported mathematical model*, PLoS One, 6 (2011), e24225.
- [5] D. ANGELI, M. ALIAL-RADHAWI, AND E. SONTAG, *A robust Lyapunov criterion for nonoscillatory behaviors in biological interaction networks*, IEEE Trans. Automat. Control, 67 (2022), pp. 3305–3320.
- [6] D. ANGELI AND E. D. SONTAG, *Monotone control systems*, IEEE Trans. Automat. Control, 48 (2003), pp. 1684–1698.
- [7] M. ARCAK, *Pattern formation by lateral inhibition in large-scale networks of cells*, IEEE Trans. Automat. Control, 58 (2013), pp. 1250–1262.
- [8] J. ARPÒN, K. SAKAI, V. GAUDIN, AND P. ANDREY, *Spatial modeling of biological patterns shows multi-scale organization of Arabidopsis thaliana heterochromatin*, Sci. Rep., 11 (2021), pp. 1–17.
- [9] S. ARTAVANIS-TSAKONAS AND P. SIMPSON, *Choosing a cell fate: A view from the notch locus*, Trends Genet., 7 (1991), pp. 403–408.
- [10] V. BERTRAND,  *$\beta$ -catenin-driven binary cell fate decisions in animal development*, Wiley Interdiscip. Rev. Dev. Biol., 5 (2016), pp. 377–388.
- [11] R. A. BRUALDI AND H. J. RYSER, *Combinatorial Matrix Theory*, Vol. 39, Cambridge University Press, Cambridge, 1991.
- [12] C. E. BUCKLEY AND D. ST JOHNSTON, *Apical-basal polarity and the control of epithelial form and function*, Nat. Rev. Mol. Cell Biol., 23 (2022), pp. 1–19.
- [13] J. P. CAMPANALE, T. Y. SUN, AND D. J. MONTELL, *Development and dynamics of cell polarity at a glance*, J. Cell Sci., 130 (2017), pp. 1201–1207.
- [14] K. CHANG, K. PEARSON, AND T. ZHANG, *Perron-Frobenius theorem for nonnegative tensors*, Commun. Math. Sci., 6 (2008), pp. 507–520.
- [15] S. C. CHAPRA, *Applied Numerical Methods with MATLAB for Engineers and Scientists*, McGraw-Hill, New York, 2012.
- [16] J. R. COLLIER, N. A. MONK, P. K. MAINI, AND J. H. LEWIS, *Pattern formation by lateral inhibition with feedback: A mathematical model of delta-notch intercellular signalling*, J. Theoret. Biol., 183 (1996), pp. 429–446.
- [17] G. M. COLLU, A. HIDALGO-SASTRE, AND K. BRENNAN, *Wnt-Notch signalling crosstalk in development and disease*, Cell Mol. Life Sci., 71 (2014), pp. 3553–3567.

- [18] F. DE PAULA, T. H. N. TESHIMA, R. HSIEH, M. M. SOUZA, M. M. S. NICO, AND S. V. LOURENCO, *Overview of human salivary glands: Highlights of morphology and developing processes*, *Anat. Rec.*, 300 (2017), pp. 1180–1188.
- [19] S. F. GILBERT, *Developmental Biology*, Sinauer Associates, Sunderland, MA, 2016.
- [20] C. GODSIL AND G. F. ROYLE, *Algebraic Graph Theory*, Vol. 207, Springer-Verlag, Berlin, 2001.
- [21] C. D. GODSIL, *Compact graphs and equitable partitions*, *Linear Algebra Appl.*, 255 (1997), pp. 259–266.
- [22] M. GOLUBITSKY AND I. STEWART, *Nonlinear dynamics of networks: The groupoid formalism*, *Bull. Amer. Math. Soc.*, 43 (2006), pp. 305–364.
- [23] M. GOLUBITSKY, I. STEWART, AND A. TÖRÖK, *Patterns of synchrony in coupled cell networks with multiple arrows*, *SIAM J. Appl. Dyn. Syst.*, 4 (2005), pp. 78–100.
- [24] A. GRAHAM, *Kronecker Products and Matrix Calculus with Applications*, Dover, New York, 2018.
- [25] A. GYORGY AND M. ARCAK, *Pattern formation in large-scale networks with asymmetric connections*, *IFAC-PapersOnLine*, 50 (2017), pp. 10944–10949.
- [26] A. GYORGY AND M. ARCAK, *Pattern formation over multigraphs*, *IEEE Trans. Network Sci. Eng.*, 5 (2017), pp. 55–64.
- [27] Y. HARDY AND W.-H. STEEB, *Matrix Calculus, Kronecker Product and Tensor Product: A Practical Approach to Linear Algebra, Multilinear Algebra and Tensor Calculus with Software Implementations*, World Scientific, River Edge, NJ, 2019.
- [28] M. W. HIRSCH, *Differential equations and convergence almost everywhere in strongly monotone semiflows*, *Contemp. Math.*, 17 (1983), pp. 267–285.
- [29] B. L. HOGAN AND P. A. KOLODZIEJ, *Molecular mechanisms of tubulogenesis*, *Nat. Rev. Genet.*, 3 (2002), pp. 513–523.
- [30] W. HORSTHEMKE, K. LAM, AND P. K. MOORE, *Network topology and turing instabilities in small arrays of diffusively coupled reactors*, *Phys. Lett. A*, 328 (2004), pp. 444–451.
- [31] J. M. HOWIE, *Real Analysis*, Springer-Verlag, Berlin, 2006.
- [32] T. JARDÉ, B. LLOYD-LEWIS, M. THOMAS, H. KENDRICK, L. MELCHOR, L. BOUGARET, P. D. WATSON, K. EWAN, M. J. SMALLEY, AND T. C. DALE, *Wnt and Neuregulin1/ErbB signalling extends 3d culture of hormone responsive mammary organoids*, *Nat. Commun.*, 7 (2016), pp. 1–14.
- [33] L. JIMENEZ-ROJO, Z. GRANCHI, D. GRAF, AND T. A. MITSIADIS, *Stem cell fate determination during development and regeneration of ectodermal organs*, *Front. Physiol.*, 3 (2012), 107.
- [34] C. R. JOHNSON, *Row stochastic matrices similar to doubly stochastic matrices*, *Linear Multilinear Algebra*, 10 (1981), pp. 113–130.
- [35] L. JORG AND M. VOLKER, *Linear Algebra*, Springer-Verlag, Berlin, 2015.
- [36] E. KAMKE, *Zur theorie der systeme gewöhnlicher differentialgleichungen. II.*, *Acta Math.*, 58 (1932), pp. 57–85.
- [37] S. K. KAY, H. A. HARRINGTON, S. SHEPHERD, K. BRENNAN, T. C. DALE, J. M. OSBORNE, D. J. GAVAGHAN, AND H. M. BYRNE, *The role of the Hes1 crosstalk hub in Notch-Wnt interactions of the intestinal crypt*, *PLoS Comp. Biol.*, 13 (2017), e1005400.
- [38] E. KLIPP AND W. LIEBERMEISTER, *Mathematical modeling of intracellular signaling pathways*, *BMC Neurosci.*, 7 (2006), pp. 1–16.
- [39] A. L. KRAUSE, E. A. GAFFNEY, P. K. MAINI, AND V. KLIKA, *Introduction to “recent progress and open frontiers in Turing’s theory of morphogenesis,”* *Philos. Trans. Roy. Soc. A*, 379 (2021), 20200280.
- [40] D. KUMAR, *Advanced Calculus of Several Variables*, Alpha Science International Ltd., Oxford, 2014.
- [41] R. KURATA, S. FUTAKI, I. NAKANO, A. TANEMURA, H. MUROTA, I. KATAYAMA, AND K. SEKIGUCHI, *Isolation and characterization of sweat gland myoepithelial cells from human skin*, *Cell Struct. Funct.*, 39 (2014), pp. 101–112.
- [42] G. LEONI, *A First Course in Sobolev Spaces*, American Mathematical Society, Providence, RI, 2017.
- [43] A. M. LILJA, V. RODILLA, M. HUYGHE, E. HANNEZO, C. LANDRAGIN, O. RENAUD, O. LEROY, S. RULANDS, B. D. SIMONS, AND S. FRE, *Clonal analysis of notch1-expressing cells reveals the existence of unipotent stem cells that retain long-term plasticity in the embryonic mammary gland*, *Nat. Cell Biol.*, 20 (2018), pp. 677–687.
- [44] B. LLOYD-LEWIS, P. MOURIKIS, AND S. FRE, *Notch signalling: Sensor and instructor of the microenvironment to coordinate cell fate and organ morphogenesis*, *Curr. Opin. Cell Biol.*, 61 (2019), pp. 16–23, <https://doi.org/10.1016/j.ceb.2019.06.003>.

- [45] J. W. MOORE, T. C. DALE, AND T. E. WOOLLEY, *Polarity-driven laminar pattern formation by lateral inhibition in 2d and 3d bilayer geometries*, IMA J. Appl. Math., 87 (2022), pp. 568–606.
- [46] P. K. MOORE AND W. HORSTHEMKE, *Localized patterns in homogeneous networks of diffusively coupled reactors*, Phys. D, 206 (2005), pp. 121–144.
- [47] F. MOTEGI, N. PLACHTA, AND V. VIASNOFF, *Novel approaches to link apicobasal polarity to cell fate specification*, Curr. Opin. Cell Biol., 62 (2020), pp. 78–85.
- [48] J. D. MURRAY, *Mathematical Biology I: An Introduction*, Springer-Verlag, Berlin, 2002.
- [49] J. D. MURRAY, *Mathematical Biology II: Spatial Models and Biomedical Applications*, Springer-Verlag, Berlin, 2003.
- [50] S. OKUDA, T. MIURA, Y. INOUE, T. ADACHI, AND M. EIRAKU, *Combining Turing and 3d vertex models reproduces autonomous multicellular morphogenesis with undulation, tubulation, and branching*, Sci. Rep., 8 (2018), pp. 1–15.
- [51] N. PERRIMON, C. PITSOULI, AND B.-Z. SHILO, *Signaling mechanisms controlling cell fate and embryonic patterning*, Cold Spring Harb. Perspect. Biol., 4 (2012), a005975.
- [52] A. S. RUFINO FERREIRA AND M. ARCAK, *Graph partitioning approach to predicting patterns in lateral inhibition systems*, SIAM J. Appl. Dyn. Syst., 12 (2013), pp. 2012–2031.
- [53] M. SÁEZ, J. BRISCOE, AND D. RAND, *Dynamical landscapes of cell fate decisions*, Interface Focus, 12 (2022), 20220002.
- [54] K. SAGA, *Structure and function of human sweat glands studied with histochemistry and cytochemistry*, Prog. Histochem. Cytochem., 37 (2002), pp. 323–386.
- [55] M. SJÖQVIST AND E. R. ANDERSSON, *Do as I say, Not(ch) as I do: Lateral control of cell fate*, Dev. Biol., 447 (2019), pp. 58–70.
- [56] H. L. SMITH, *Periodic solutions of periodic competitive and cooperative systems*, SIAM J. Math. Anal., 17 (1986), pp. 1289–1318.
- [57] H. L. SMITH, *Monotone Dynamical Systems: An Introduction to the Theory of Competitive and Cooperative Systems*, American Mathematical Society, Providence, RI, 2008.
- [58] D. SPRINZAK, A. LAKHANPAL, L. LEBON, L. A. SANTAT, M. E. FONTES, G. A. ANDERSON, J. GARCIA-OJALVO, AND M. B. ELOWITZ, *Cis-interactions between Notch and Delta generate mutually exclusive signalling states*, Nature, 465 (2010), pp. 86–90.
- [59] I. STEWART, M. GOLUBITSKY, AND M. PIVATO, *Symmetry groupoids and patterns of synchrony in coupled cell networks*, SIAM J. Appl. Dyn. Syst., 2 (2003), pp. 609–646.
- [60] J. SUMBAL, A. CHICHE, E. CHARIFOU, Z. KOLEDOVA, AND H. LI, *Primary mammary organoid model of lactation and involution*, Front. Cell Dev. Biol., 8 (2020), 68.
- [61] A. M. TURING, *The chemical basis of morphogenesis*, Philos. Trans. Roy. Soc. London Ser. B, 237 (1952), pp. 37–72.
- [62] S. VORHAGEN AND C. M. NIESSEN, *Mammalian aPKC/Par polarity complex mediated regulation of epithelial division orientation and cell fate*, Exp. Cell Res., 328 (2014), pp. 296–302.
- [63] A. J. WAGERS, J. L. CHRISTENSEN, AND I. WEISSMAN, *Cell fate determination from stem cells*, Gene Ther., 9 (2002), pp. 606–612.
- [64] H. J. WEARING, M. R. OWEN, AND J. A. SHERRATT, *Mathematical modelling of juxtacrine patterning*, Bull. Math. Biol., 62 (2000), pp. 293–320.
- [65] H. J. WEARING AND J. A. SHERRATT, *Nonlinear analysis of juxtacrine patterns*, SIAM J. Appl. Math., 62 (2001), pp. 283–309.
- [66] L. WOLPERT, C. TICKLE, AND A. M. ARIAS, *Principles of Development*, Oxford University Press, Oxford, 2015.
- [67] T. E. WOOLLEY, R. E. BAKER, AND P. K. MAINI, *Turing’s theory of morphogenesis: Where we started, where we are and where we want to go*, in *The Incomputable*, Springer-Verlag, Berlin, 2017, pp. 219–235.
- [68] T. E. WOOLLEY, A. L. KRAUSE, AND E. A. GAFFNEY, *Bespoke turing systems*, Bull. Math. Biol., 83 (2021), pp. 1–32.
- [69] F. ZHANG, *Matrix Theory: Basic Results and Techniques*, Springer-Verlag, Berlin, 2011.